

The mass spectrum of compact remnants from the PARSEC stellar evolution tracks

Mario Spera,¹★ Michela Mapelli^{1,2} and Alessandro Bressan^{1,3}

¹INAF, Osservatorio Astronomico di Padova, Vicolo dell'Osservatorio 5, I-35122 Padova, Italy

²INFN, Milano Bicocca, Piazza della Scienza 3, I-20126 Milano, Italy

³Scuola Internazionale Superiore di Studi Avanzati (SISSA), Via Bonomea 265, I-34136 Trieste, Italy

Accepted 2015 May 18. Received 2015 May 15; in original form 2015 March 2

ABSTRACT

The mass spectrum of stellar mass black holes (BHs) is highly uncertain. Dynamical mass measurements are available only for few (~ 10) BHs in X-ray binaries, while theoretical models strongly depend on the hydrodynamics of supernova (SN) explosions and on the evolution of massive stars. In this paper, we present and discuss the mass spectrum of compact remnants that we obtained with *SEVN*, a new public population-synthesis code, which couples the *PARSEC* stellar evolution tracks with up-to-date recipes for SN explosion (depending on the carbon–oxygen mass of the progenitor, on the compactness of the stellar core at pre-SN stage and on a recent two-parameter criterion based on the dimensionless entropy per nucleon at pre-SN stage). *SEVN* can be used both as a stand-alone code and in combination with direct-summation *N*-body codes (*STARLAB*, *HIGPUS*). The *PARSEC* stellar evolution tracks currently implemented in *SEVN* predict significantly larger values of the carbon–oxygen core mass with respect to previous models. For most of the SN recipes we adopt, this implies substantially larger BH masses at low metallicity ($\leq 2 \times 10^{-3}$), than other population synthesis codes. The maximum BH mass found with *SEVN* is ~ 25 , 60 and $130 M_{\odot}$ at metallicity $Z = 2 \times 10^{-2}$, 2×10^{-3} and 2×10^{-4} , respectively. Mass loss by stellar winds plays a major role in determining the mass of BHs for very massive stars ($\geq 90 M_{\odot}$), while the remnant mass spectrum depends mostly on the adopted SN recipe for lower progenitor masses. We discuss the implications of our results for the transition between neutron star and BH mass, and for the expected number of massive BHs (with mass $> 25 M_{\odot}$) as a function of metallicity.

Key words: black hole physics – methods: numerical – stars: evolution – stars: mass-loss – stars: neutron.

1 INTRODUCTION

Compact remnants are the final stage of the evolution of massive stars, and power a plethora of important astrophysical processes: they are the engine of the X-ray binaries we observe in the nearby Universe, and may be powerful sources of gravitational waves (e.g. Phinney 1991). Furthermore, the merger of two neutron stars (NSs) and/or that of a stellar black hole (BH) with a NS are expected to lead to one of the most energetic transient phenomena in the Universe: the short gamma-ray bursts (e.g. Paczynski 1991). Finally, X-ray binaries powered by BHs and/or NSs are the key to explain some of the most luminous point-like non-nuclear X-ray sources (the ultraluminous X-ray sources; e.g. Mapelli et al. 2010; Mapelli & Zampieri 2014 and references therein), and are an important source of feedback, in both the nearby and the early Universe (e.g. Justham & Schawinski 2012, and references therein).

Despite their importance for astrophysics, the details of the formation of BHs and NSs (and especially the link with their progenitor stars) are matter of debate. From the observational point of view, the confirmed BHs are only a few tens (see table 2 of Özel et al. 2010, for one of the most updated compilations). These are located in X-ray binaries, mostly in the Milky Way (MW), and an accurate dynamical mass estimate has been derived only for a fraction of them (~ 10). Most of the derived BH masses are in the range $5 \leq m_{\text{BH}}/M_{\odot} \leq 10$. In the MW, the most massive BHs in X-ray binaries do not significantly exceed $m_{\text{BH}} \sim 15 M_{\odot}$, whereas a few BHs in nearby galaxies might have higher masses: M33 X-7 ($m_{\text{BH}} = 15.65 \pm 1.45 M_{\odot}$; Orosz et al. 2007), IC 10 X-1 ($m_{\text{BH}} \sim 23\text{--}34 M_{\odot}$; Prestwich et al. 2007; Silverman & Filippenko 2008), NGC 300 X-1 ($m_{\text{BH}} > 10 M_{\odot}$; Crowther et al. 2007, 2010). Interestingly, these three massive BHs are in regions with relatively low metallicity. A metallicity $Z \sim 0.004$ is estimated for the dwarf irregular galaxy IC 10 (Garnett 1990). The metallicity of M33 in proximity of X-7 is $Z \sim 0.008$, and that of NGC 300 in proximity of X-1 is $Z \sim 0.006$ (Pilyugin, Vílchez & Contini 2004).

★E-mail: mario.spera@live.it

The statistics is significantly larger for NSs: currently, there are dynamical mass measurements for 61 NSs (17, 11, 30 and 3 of them are in X-ray binaries, NS–NS binaries, NS–white dwarf (WD) binaries and NS–main-sequence (MS) binaries, respectively, <http://stellarcollapse.org/nsmasses>; Lattimer & Prakash 2005; Lattimer 2012).

The link between the progenitor star and the compact remnant is still poorly constrained for both BHs and NSs: observations of core-collapse supernovae (SNe) indicate a deficit of massive ($\gtrsim 20 M_{\odot}$) progenitor stars (Smartt 2009; Horiuchi et al. 2011; Jennings et al. 2012, 2014; Gerke, Kochanek & Stanek 2015), which possibly suggests that the most massive stars undergo no or faint SNe.

From a theoretical perspective, the formation and the mass spectrum of BHs and NSs strongly depend on two fundamental processes: (i) the hydrodynamics of SNe; (ii) mass loss by stellar winds in massive stars (during and especially after the MS).

(i) The physics of SN explosions is extremely complex, and the hydrodynamical codes that investigate the explosion mechanisms are computationally challenging (see e.g. Fryer 1999, 2006; Fryer & Kalogera 2001; Heger & Woosley 2002; Heger et al. 2003; O’Connor & Ott 2011; Fryer et al. 2012; Janka 2012; Ugliano et al. 2012; Burrows 2013; Ertl et al. 2015; Pejcha & Prieto 2015). In particular, the link between the late evolutionary stages of a massive star and the SN products is still matter of debate. Several authors (e.g. Bethe 1990; Janka et al. 2007; Janka 2012; Burrows 2013) investigate for which structural properties of the progenitor star a SN can fail, leading to the direct collapse of the star to a BH. Even if the SN occurs, how much matter can fall back and be accreted on to the protocompact remnant is very uncertain.

(ii) For massive progenitors (zero-age MS mass $M_{\text{ZAMS}} \geq 30 M_{\odot}$) the details of stellar evolution are very important for the SN outcome and for the final remnant mass. In fact, the final mass M_{fin} of the progenitor star (i.e. the mass of a star immediately before the collapse) is governed by the amount of mass loss by stellar winds (e.g. Mapelli, Colpi & Zampieri 2009; Belczynski et al. 2010; Fryer et al. 2012; Mapelli et al. 2013). The rate of mass loss by stellar winds on the MS increases with the metallicity of the star as $\dot{M} \propto Z^{\alpha}$, where $\alpha \sim 0.5\text{--}0.9$, depending on the model (e.g. Kudritzki, Pauldrach & Puls 1987; Leitherer, Robert & Drissen 1992; Kudritzki & Puls 2000; Vink, de Koter & Lamers 2001; Kudritzki 2002). The behaviour of evolved massive stars, such as luminous blue variable stars (LBVs) and Wolf–Rayet stars (WRs), is also expected to depend on metallicity, but with larger uncertainties (e.g. Meynet & Maeder 2005; Vink & de Koter 2005; Bressan et al. 2012; Tang et al. 2014).

Both the models of SN explosion (e.g. Fryer et al. 2012; Janka 2012; Burrows 2013; Clausen et al. 2015; Ertl et al. 2015; Pejcha & Prieto 2015) and the theory of massive star evolution (e.g. Bressan et al. 2012; Tang et al. 2014) were deeply revised in the last few years. For these reasons, population synthesis codes that aim at studying the demographics of compact remnants must account for up-to-date models for both SN explosions and stellar evolution. Here we present *SEVN* (acronym for ‘Stellar EVolution *N*-body’), a new population synthesis tool that couples *PARSEC* evolutionary tracks for stellar evolution (Bressan et al. 2012; Chen et al. 2014; Tang et al. 2014) with up-to-date models for SN explosion (Fryer et al. 2012; Janka 2012; Ertl et al. 2015), and that can be easily merged with several *N*-body codes. The new *PARSEC* evolutionary tracks consider the most recent updates for mass loss by stellar winds and other input physics. In this paper, we present and discuss the mass

spectrum of BHs and NSs that we obtain from *SEVN*, with particular attention to the dependence of the remnant mass on metallicity.

Furthermore, *SEVN* is extremely versatile, because it relies upon a set of tables extracted from stellar evolution tracks: if we are interested in comparing different stellar evolution models, we can do it quickly and easily, by changing tables. The new tool is publicly available.¹ *SEVN* is specifically designed to add updated recipes for stellar evolution and SN explosion to *N*-body simulations, even though it can be used as a simple and fast stand-alone population synthesis code too. In particular, we merged it with the *STARLAB* public software environment (Portegies Zwart et al. 2001) and with an upgraded version of *HIGPUS* code (Capuzzo-Dolcetta, Spera & Punzo 2013; Spera, in preparation). Thus, the new code can be used for both population synthesis studies of compact object binaries in the field, and for investigating the dynamical evolution of compact objects in star clusters. The evolution of compact remnants in star clusters is of crucial importance, since star clusters are sites of intense dynamical processes, which may significantly affect the formation of X-ray binaries (e.g. Blecha et al. 2006; Mapelli et al. 2013; Mapelli & Zampieri 2014), as well as the formation and merger of double-compact object binaries (e.g. O’Leary et al. 2006; Sadowski et al. 2008; Downing et al. 2010, 2011; Ziosi et al. 2014). Furthermore, extreme dynamical processes, such as repeated mergers of compact remnants (Miller & Hamilton 2002) and the runaway merger of massive objects in star clusters (Portegies Zwart & McMillan 2002), can lead to the formation of intermediate-mass BHs (i.e. BHs with mass $10^2\text{--}10^5 M_{\odot}$). Finally, compact remnants are also expected to affect the overall dynamical evolution of star clusters (Downing 2012; Sippel et al. 2012; Mapelli & Bressan 2013; Trani, Mapelli & Bressan 2014).

This paper is organized as follows. In Section 2, we describe the main features and ingredients of *SEVN* (including stellar evolution and SN models). In Section 3, we discuss the outputs of *SEVN*, with particular attention to the mass spectrum and the mass function of NSs and BHs. Furthermore, we compare the results of *SEVN* with those of other population synthesis codes. In Section 4, we discuss the results we obtained applying the O’Connor & Ott (2011) and Ertl et al. (2015) prescriptions for SN explosion to *PARSEC* progenitors, at metallicity $Z = 0.02$. In Section 5, we summarize our main results.

2 METHOD

2.1 Single stellar evolution with PARSEC

The *PARSEC* data base includes updated and homogeneous sets of canonical single stellar evolutionary tracks, from very low ($M = 0.1 M_{\odot}$) to very massive ($M = 350 M_{\odot}$) stars, and from the pre-MS to the beginning of central carbon burning. The code is thoroughly discussed in Bressan et al. (2012, 2013), Chen et al. (2014) and Tang et al. (2014) and here we briefly describe its most important characteristics. The equation of state (EOS) is computed with the *FREEEOS* code² (A. W. Irwin). Opacities are computed combining the high-temperature data from the Opacity Project At Lawrence Livermore National Laboratory (OPAL; Iglesias & Rogers 1996) with the low-temperature data from the *ÆSOPUS*³ code (Marigo & Aringer 2009). Conductive opacities are included following Itoh et al. (2008). The

¹ *SEVN* upon request to the authors, through the email mario.spera@oapd.inaf.it or mario.spera@live.it

² <http://freeeos.sourceforge.net/>

³ <http://stev.oapd.inaf.it/aesopus>

main hydrogen and helium burning reactions are included as recommended in the JINA data base (Cyburt et al. 2010) with electron screening factors taken from Dewitt, Graboske & Cooper (1973) and Graboske et al. (1973). Energy losses by electron neutrinos are taken from Itoh & Kohyama (1983), Munakata, Kohyama & Itoh (1985) and Haft, Raffelt & Weiss (1994). Instability against convection is tested by means of the Schwarzschild criterion and, where needed, the convective temperature gradient is estimated with the mixing length theory of Böhm-Vitense (1958) with a mixing length parameter calibrated on the solar model, $\alpha_{\text{MLT}} = 1.74$. The location of the boundary of the convective core is estimated in the framework of the mixing length theory, allowing for the penetration of convective elements into the stable regions (Bressan, Chiosi & Bertelli 1981). As thoroughly described in Bressan et al. (2013), the main parameter describing core overshooting is the mean free path of convective elements across the border of the unstable region $l_c = \Lambda_c H_P$ with $\Lambda_c = 0.5$, as result of the calibration obtained by the analysis of intermediate-age clusters (Girardi, Rubele & Kerber 2009) as well as individual stars (Deheuvels et al. 2010; Kamath et al. 2010; Torres et al. 2014). Effects of stellar rotation have not yet been introduced in PARSEC.

The reference solar partition of heavy elements is taken from Caffau et al. (2011) who revised a few species of the Grevesse & Sauval (1998) compilation. According to Caffau et al. (2011) compilation, the present-day Sun’s metallicity is $Z_{\odot} = 0.01524$.

While the evolution below $M = 12 M_{\odot}$ is computed at constant mass, for more massive stars the mass-loss rate is taken into account combining the mass-loss rates formulations provided by different authors for different evolutionary phases, as described in Tang et al. (2014). During the blue supergiant (BSG) and LBV phases we adopt the maximum between the relations provided by Vink, de Koter & Lamers (2000, 2001), and that provided by Vink et al. (2011) which includes the dependence of the mass-loss rates on the ratio (Γ) of the star luminosity to the corresponding Eddington luminosity. In the red supergiant (RSG) phases we adopt the mass-loss rates by de Jager, Nieuwenhuijzen & van der Hucht (1988), R_{dJ} , while, in the WR phases, we use the Nugis & Lamers (2000) formalism.

An important effect of the metallicity is its modulation of the mass-loss rates. As discussed in Tang et al. (2014) and in Chen et al. (in preparation), the dependence of the radiation-driven mass-loss rates on the metallicity is a strong function of Γ . While, at low values of Γ , the mass-loss rates obey the relation $\dot{M} \propto (Z/Z_{\odot})^{0.85} M_{\odot} \text{ yr}^{-1}$ (Vink et al. 2000, 2001), with $Z_{\odot} = 0.02$ being the average metallicity assumed for Galactic massive stars, at increasing Γ the metallicity dependence becomes weaker, and it disappears as Γ approaches 1 (Gräfener & Hamann 2008). Tang et al. (2014) show that the metallicity effect can be expressed as

$$\dot{M} \propto (Z/Z_{\odot})^{\alpha}, \quad (1)$$

with the coefficient α determined from a fit to the published relationships by Gräfener & Hamann (2008):

$$\begin{aligned} \alpha &= 0.85 & (\Gamma < 2/3), \\ \alpha &= 2.45 - 2.4 \Gamma & (2/3 \leq \Gamma \leq 1). \end{aligned} \quad (2)$$

In the WR phases, PARSEC makes use of the Nugis & Lamers (2000) formalism, with its own dependence on the stellar metallicity while, during the RSG phases the de Jager et al. (1988) rates are re-scaled adopting the usual relation $\dot{M} \propto (Z/Z_{\odot})^{0.85} M_{\odot} \text{ yr}^{-1}$.

With these assumptions for the mass-loss rates, the new models of near-solar metallicity can naturally reproduce the observed lack of supergiant stars above the Humphreys & Davidson (1979) limit.

The lack of RSG stars is usually interpreted as a signature of the effects of enhanced mass-loss rates when the star enter this region, and this interpretation is supported by the presence, around this limit, of LBV stars which are known to be characterized by high mass-loss rates. While, in previous models, the limit was reproduced by adopting an ‘ad hoc’ enhancement of the mass-loss rates, in the current models the enhancement is nicely reproduced by the boosting of the mass-loss rate when the stars approach the Eddington limit (Chen et al., in preparation). At metallicities lower than solar, the boosting is mitigated by the reduction factor introduced by the metallicity dependence. At $Z = 0.001$, the upper MS widens significantly and the more massive stars evolve in the ‘forbidden’ region even during the H-burning phase, because of their very large convective cores. They may also ignite and burn central helium as ‘red’ supergiant stars. The full set of new evolutionary tracks and the corresponding isochrones may be found at <http://people.sissa.it/sbressan/parsec.html> and <http://stev.oapd.inaf.it/cgi-bin/cmd>, respectively.

2.2 SEVN general description

The coupling between dynamics and stellar evolution, in a single code, can be achieved through three alternative approaches.

(i) The first one is based on a ‘brute force’ approach. It consists in calling an advanced stellar evolution code (such as PARSEC) that calculates the detailed evolution of stellar physical parameters step-by-step, following the time intervals imposed by the N -body dynamics.

(ii) The second one is based on polynomial fittings that interpolate the fundamental stellar parameters (radius, luminosity, temperature and chemical composition), as a function of time, mass and metallicity. Besides being a fast choice in terms of computing time, one of the main advantages of using this strategy is that it can be implemented with little effort.

(iii) The third approach consists in using stellar evolution isochrones as input files. These isochrones are usually provided in the form of tables, for a grid of masses and metallicities, and they are read and interpolated by the numerical code on the fly. The main advantage of this strategy is that it makes the implementation more general. The option to change the built-in stellar evolution recipes is left to users, who can substitute the input tables, without modifying the internal structure of the code or even recompiling it.

The first approach is highly inefficient because the continuous calls to advanced stellar evolution codes, inside an N -body integrator, significantly slows down the overall numerical evolution. To develop SEVN, we chose to follow the second aforementioned approach (usage of stellar evolution isochrones in tabular form). SEVN can work as a stand-alone code (for fast population synthesis studies in the field), and can be linked to a large variety of N -body codes, without suffering a performance penalty. In particular, we merged SEVN with an updated version of the direct N -body code HIGPUS⁴ (Capuzzo-Dolcetta et al. 2013; Spera, in preparation) as well as in the STARLAB software environment⁵ (Portegies Zwart et al. 2001), and it can also be included in the Astrophysical Multipurpose Software Environment (AMUSE;⁶ Pelupessy et al. 2013).

In this paper, we focus our attention on our implementation of SEVN in STARLAB since it already includes both an N -body integrator

⁴ <http://astrowww.phys.uniroma1.it/dolcetta/HPCcodes/HiGPUs.html>

⁵ <http://www.sns.ias.edu/starlab/>

⁶ <http://amusecode.org/wiki>

(called KIRA) and a binary evolution module (SEBA). In particular, we updated a version of SEBA that had been previously modified by Mapelli et al. (2013), who included metallicity-dependent stellar winds (Hurley, Pols & Tout 2000) and prescriptions for the mass loss by MS stars (Vink et al. 2001). While we left the dynamical integration part untouched, we rearranged SEBA by adding stellar isochrone tables, at different metallicity, and by forcing the software to use them as input files. In this way, we have hidden the default implementation without making radical changes to the code structure. In the current version of SEVN, we use the PARSEC data to get the physical parameters of the stars for all evolutionary stages but the thermally pulsating AGB (TP-AGB) phase. In fact, the evolution and lifetimes of TP-AGB stars suffer from significant uncertainties and a thorough calibration of the latter phase is still underway (Marigo et al. 2013; Rosenfield et al. 2014). At present, we use the built-in SEBA SUPER_GIANT class to follow the evolution of the stars in this stage. Moreover, according to the PARSEC recipes, all stars with an initial mass $M_{\text{ZAMS}} \lesssim M_{\text{up}}$ (with $M_{\text{up}} = 7 M_{\odot}$) undergo the AGB phase. In particular, at the end of their lives, stars of mass $M_{\text{ZAMS}} \gtrsim M_{\text{up}}$ will explode as SNe leaving NSs or BHs as compact remnants, while stars with $M_{\text{ZAMS}} < M_{\text{up}}$ will evolve through the AGB phase, quickly losing their envelopes, until a WD is formed. More technical details about the SEVN implementation can be found in Appendix A.

2.3 Prescriptions for the formation of compact remnants

The default recipes implemented in the SEBA module predict the formation of a WD if the final core mass is less than the Chandrasekhar mass ($1.4 M_{\odot}$), a NS or a BH if the core mass is greater than $1.4 M_{\odot}$. In our implementation of SEVN in SEBA, we leave the recipes for the formation of WDs unchanged, but we change the way to form NSs and BHs.

The default version of SEBA distinguishes between NSs and BHs by inspecting the final mass of the core: if it is larger than the Chandrasekhar mass ($1.4 M_{\odot}$) and, at the same time, the initial mass of the star is $M_{\text{ZAMS}} < 25 M_{\odot}$, a NS is formed. If $M_{\text{ZAMS}} \geq 25 M_{\odot}$ or if the final carbon–oxygen (CO) core mass (M_{CO}) is such that $M_{\text{CO}} \geq 5 M_{\odot}$, the star ends its life forming a BH.⁷ To determine the BH mass, SEBA assumes that, initially, a fixed amount of the CO core mass collapses, forming a protocompact object of mass $M_{\text{proto}} = 3 M_{\odot}$ (Fryer & Kalogera 2001). The amount of fallback material, M_{fb} , is determined by comparing the binding energies of the hydrogen (H), helium (He) and CO shells with the SN explosion energy. The final mass of the compact object is given by $M_{\text{BH}} = M_{\text{proto}} + M_{\text{fb}}$.

In SEVN, we substituted the default SEBA treatment of SNe with the following new recipes. We implemented the three models described in details by Fryer et al. (2012): (i) the model implemented in the STARTRACK population synthesis code (see Belczynski et al. 2008, 2010); (ii) the *rapid supernova model* and (iii) the *delayed supernova model*. The main difference between the last two explosion mechanisms is the time-scale over which the explosion occurs: < 250 ms after the bounce for the rapid model, $\gtrsim 0.5$ s for the delayed mechanism (for the details see e.g. Bethe 1990). A common feature of these models is that they depend only on the final characteristics of the star, by means of the final CO core mass (M_{CO}) and of

the final mass of the star (M_{fin}). Appendix B summarizes the main features of the Fryer et al. (2012) SN explosion recipes. We recall that the Fryer et al. (2012) methods are general prescriptions for the formation of compact remnants, and do not distinguish, a priori, between NSs and BHs. In SEVN, we assume that all the remnants with masses $M_{\text{rem}} < 3.0 M_{\odot}$ are NSs, and that the objects with masses $M_{\text{rem}} \geq 3.0 M_{\odot}$ are BHs, according to the maximum mass of a NS indicated by the Tolman–Oppenheimer–Volkoff limit (Oppenheimer & Volkoff 1939). While the Fryer et al. (2012) models are extremely simple to implement in a population synthesis code, it has been recently suggested that the dependence of the mass of the compact remnant on M_{fin} or M_{CO} might be significantly more complex (O’Connor & Ott 2011; Janka 2012; Ugliano et al. 2012; Sukhbold & Woosley 2014; Smartt 2015). The internal structure of stars, at core-collapse stage, may exhibit significant differences, leading to deep changes on the physical parameters of compact remnants, even if the progenitors are very close in terms of M_{ZAMS} or M_{CO} . As a consequence, an one-to-one relation between the mass of the compact remnant and e.g. M_{CO} could be inadequate to discriminate between SNe (formation of a NS) and failed SNe (direct collapse to a BH). The critical parameter to distinguish between SNe and failed SNe might be the compactness of stellar cores at the pre-SN stage (O’Connor & Ott 2011; Ugliano et al. 2012; Sukhbold & Woosley 2014). Alternatively one may use an equivalent criterion based on the two parameters M_4 , representing the enclosed mass at a dimensionless entropy per nucleon $s = 4$, and μ_4 , that is the mass gradient at the same location (Ertl et al. 2015). In order to fulfil these recent advances of the SN explosion models and to test their impact on the mass spectrum of compact remnants, we have implemented in SEVN these two additional SN explosion recipes, namely the criterion based on the compactness of stellar cores (O’Connor & Ott 2011; Ugliano et al. 2012; Sukhbold & Woosley 2014) and the criterion based on M_4 and μ_4 (Ertl et al. 2015). We present here only the results for $Z = 0.02$, because the results at metallicities lower than solar are still under investigation.

In SEVN, we set the delayed SN model as default SN explosion mechanism, but the user can choose one of the aforementioned mechanisms by modifying the input parameter file. Only for the SEVN implementation in STARLAB, we also leave the choice to use the SEBA built-in recipes.⁸

Furthermore, the aforementioned models do not account for the possibility that the progenitor undergoes a pair-instability SN (e.g. Woosley, Heger & Weaver 2002). In SEVN, we add the option to activate pair-instability SNe, when the helium core mass (after the He core burning phase) is $60 \leq M_{\text{He}}/M_{\odot} \leq 133$. For this range of He core masses, the star does not leave any remnant, while it directly collapses to BH for larger masses. In the following section, we show models that do not undergo pair-instability SNe.

When a compact remnant is formed, it also receives a velocity kick, W_{kick} , due to the asymmetries that can occur during the collapse process. In SEVN, we determine the absolute value of the kick using the three-dimensional velocity distribution of the pulsars observed in our Galaxy. For details, we refer to Hobbs et al. (2005), who studied the proper motions of 233 pulsars, obtaining a Maxwellian fit for their velocity distribution, with a one-dimensional variance equal to 256 km s^{-1} . The direction of the kick is randomly chosen.

⁷ In SEBA, the limits 25 and $5 M_{\odot}$ are the default values of two parameters called SUPER_GIANT2BLACK_HOLE and COCORE2BLACK_HOLE, respectively. The user can adjust them at choice.

⁸ The first line of the file INPUT_PARAM.TXT determines the SN explosion model that will be adopted throughout the numerical simulation. It can be DELAYED, STARTRACK, RAPID, COMPACTNESS or TWOPARAMETERS. In the implementation of SEVN in STARLAB, this line can be even DEFAULT if we want to use the SEBA built-in recipes for SN explosion.

Furthermore, following the prescriptions given in Fryer et al. (2012), we also included the dependence of the velocity kick on the amount of mass that falls back on to the protocompact object. Specifically, the actual value of the kick imparted to a compact remnant, V_{kick} , is given by

$$V_{\text{kick}} = (1 - f_{\text{fb}}) W_{\text{kick}}. \quad (3)$$

Thus, a BH that forms via direct collapse ($f_{\text{fb}} = 1$) does not receive a velocity kick, while full kicks are assigned to compact remnants formed with no fallback. Another possible treatment for BH kick velocities is to assume that BHs follow the same distribution of W_{kick} as NSs, but normalized to $\langle M_{\text{NS}} \rangle / M_{\text{BH}}$ (where $\langle M_{\text{NS}} \rangle$ is the average NS mass), to ensure momentum conservation. We leave this second option in STARLAB, even if we set the former treatment as default.

3 RESULTS

In this section, we discuss the effects of metallicity on the stellar mass-loss rate, on the CO core, on the formation of compact remnants and on the mass function of NSs and BHs, as we found using our new tool SEVN. We also discuss the main differences between SEVN and other population synthesis codes, in terms of mass spectrum of compact remnants. In particular, we compare the results of SEVN with those of SSE (Hurley et al. 2000), of STARLAB (Portegies Zwart et al. 2001) and of the version of STARLAB modified by Mapelli et al. (2013) (hereafter referred as STARLABMM). In particular, SSE is a stellar evolution tool that has already been linked to the NBODYX family of N -body codes (see e.g. Aarseth 1999; Nitadori & Aarseth 2012) and it also implements recipes for metallicity-dependent stellar winds. Moreover, SSE adopts the SN explosion recipes described in Belczynski, Kalogera & Bulik (2002).

3.1 Mass loss by stellar winds

Figs 1–3 show the temporal evolution of stellar mass at $Z = 2 \times 10^{-2}$, 2×10^{-3} and 2×10^{-4} , respectively, for four selected ZAMS masses between 10 and 110 M_{\odot} . The evolution of the stellar mass predicted by PARSEC is compared with that implemented in SSE. At lower ZAMS masses ($M_{\text{ZAMS}} \lesssim 10 M_{\odot}$) the behaviour of PARSEC and SSE is almost indistinguishable.

For larger masses, there is no significant difference for most of the star's life, but there is a significant difference in the final masses M_{fin} , especially at low metallicity. The differences in M_{fin} are about 80 per cent of M_{ZAMS} for stars with $M_{\text{ZAMS}} \gtrsim 60 M_{\odot}$ at $Z = 2 \times 10^{-4}$. The reason of these differences is the treatment of stellar winds, especially in the late-MS, LBV and WR stages (see Section 2.1 and Bressan et al. 2012; Tang et al. 2014 for details).

3.2 Final mass (M_{fin}) and CO core mass (M_{CO})

The SN explosion mechanisms discussed by Fryer et al. (2012), and implemented in SEVN, depend on the final mass of the star, M_{fin} , and on its final CO mass, M_{CO} (see equations B2, B5 and B8). Since both M_{fin} and M_{CO} depend on the initial mass of the star, M_{ZAMS} , and on its metallicity, Z , thus also M_{rem} will depend on M_{ZAMS} and Z . This implies that the mass spectrum of compact remnants strongly depends on the prescriptions adopted to evolve the star until its pre-SN stage.

Fig. 4 shows the trend of M_{fin} as a function of M_{ZAMS} , for different values of the metallicity. Fig. 4 reflects the fact that metal-poor stars are subject to weaker stellar winds throughout their evolution. In

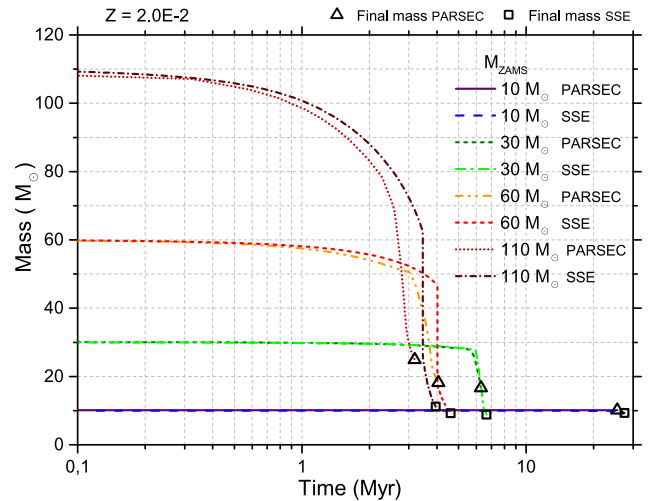


Figure 1. Temporal evolution of the stellar mass for different M_{ZAMS} and for metallicity $Z = 2.0 \times 10^{-2}$, according to PARSEC and SSE. Solid (dashed) line: evolution of a star with $M_{\text{ZAMS}} = 10 M_{\odot}$ with PARSEC (SSE); dotted (dash-dotted) line: evolution of a star with $M_{\text{ZAMS}} = 30 M_{\odot}$ with PARSEC (SSE); dash-double dotted (short dashed) line: evolution of the mass of a star with $M_{\text{ZAMS}} = 60 M_{\odot}$ with PARSEC (SSE); short dotted (short dash-dotted) line: evolution of the mass of a star with $M_{\text{ZAMS}} = 110 M_{\odot}$ with PARSEC (SSE). Open triangles and open squares mark the final point of each curve obtained using PARSEC and SSE, respectively.

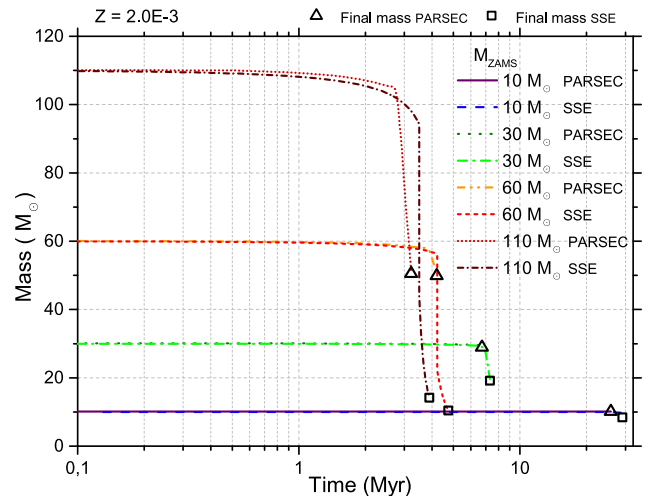


Figure 2. Same as Fig. 1, but for $Z = 2.0 \times 10^{-3}$.

fact, M_{fin} is always smaller than $\sim 25 M_{\odot}$ at $Z = 2.0 \times 10^{-2}$, while $M_{\text{fin}} \approx M_{\text{ZAMS}}$ at $Z \lesssim 2.0 \times 10^{-4}$. The curves for $Z \lesssim 2.0 \times 10^{-4}$ are well approximated by a simple linear relation

$$M_{\text{fin}}(M_{\text{ZAMS}}) = 0.9519 M_{\text{ZAMS}} + 1.45. \quad (4)$$

In Fig. 5, we show M_{CO} as a function of M_{ZAMS} , for different values of metallicity. As expected, the final CO mass scales inversely with metallicity: the maximum value of M_{CO} ranges between ~ 20 and $\sim 65 M_{\odot}$, for $1.0 \times 10^{-4} \leq Z \leq 2.0 \times 10^{-2}$. It is interesting

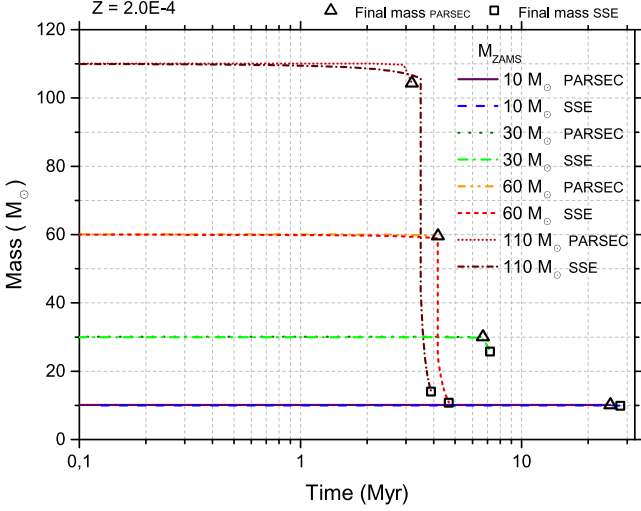


Figure 3. Same as Fig. 1, but for $Z = 2.0 \times 10^{-4}$.

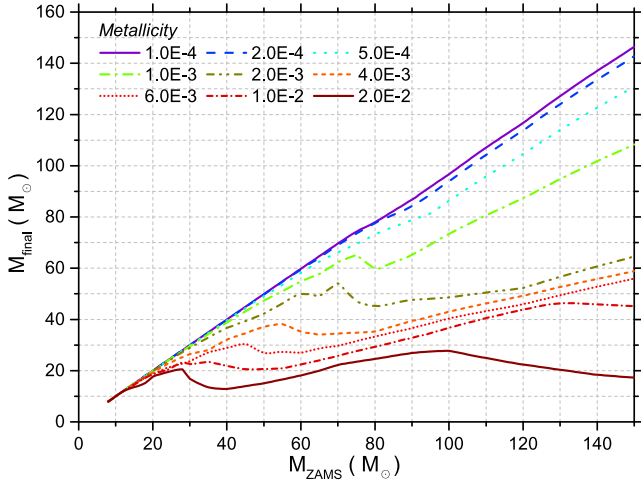


Figure 4. Final mass of the stars as a function of their initial mass, for different values of metallicity $1.0 \times 10^{-4} \leq Z \leq 2.0 \times 10^{-2}$. Top solid line: $Z = 1.0 \times 10^{-4}$; dashed line: $Z = 2.0 \times 10^{-4}$; dotted line: $Z = 5.0 \times 10^{-4}$; dash-dotted line: $Z = 1.0 \times 10^{-3}$; dash-double dotted line: $Z = 2.0 \times 10^{-3}$; short dashed line: $Z = 4.0 \times 10^{-3}$; short dotted line: $Z = 6.0 \times 10^{-3}$; short dash-dotted line: 1.0×10^{-2} ; bottom solid line: $Z = 2.0 \times 10^{-2}$.

to note that, for $Z \leq 1.0 \times 10^{-3}$, the curves of Fig. 5 become approximately independent of Z , and can be expressed as

$$M_{\text{CO}}(M_{\text{ZAMS}}) = \begin{cases} 0.3403M_{\text{ZAMS}} - 2.064 & \text{if } M_{\text{ZAMS}} < 27 M_{\odot}, \\ 0.4670M_{\text{ZAMS}} - 5.47 & \text{if } M_{\text{ZAMS}} \geq 27 M_{\odot}. \end{cases} \quad (5)$$

At present, since PARSEC does not include the TP-AGB stellar evolution phase, equation (5) holds for $M_{\text{ZAMS}} \gtrsim M_{\text{up}} = 7 M_{\odot}$ (see Section 2.2).

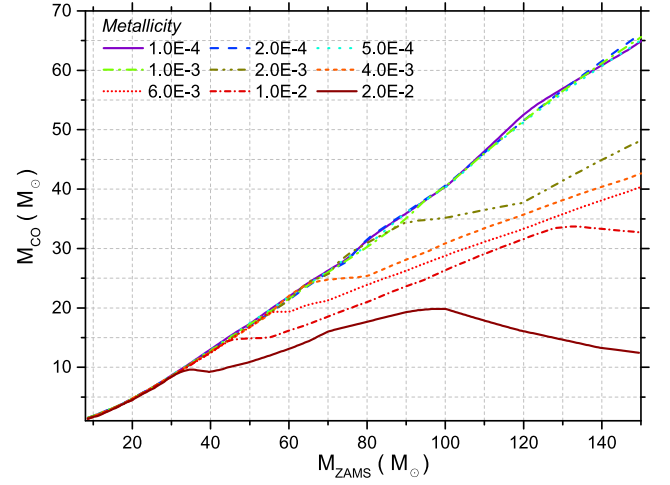


Figure 5. Final mass of the CO core as a function of the initial mass of the star, for different values of metallicity $1.0 \times 10^{-4} \leq Z \leq 2.0 \times 10^{-2}$. Line types are the same as in Fig. 4.

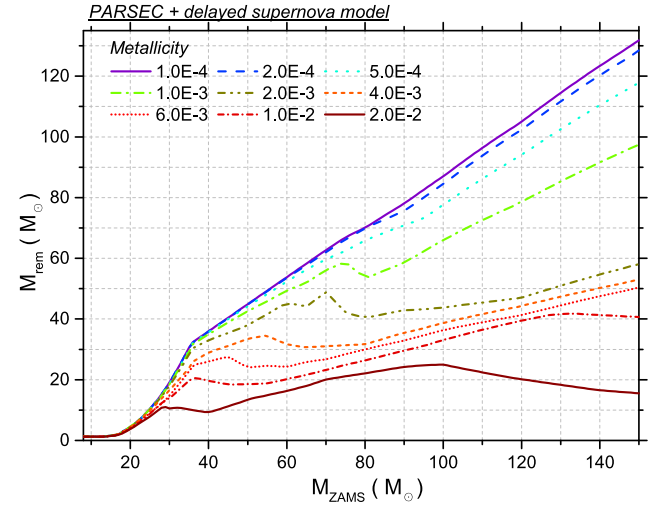


Figure 6. Mass of the final compact remnant (M_{rem}) as a function of the initial mass of the star, for various metallicities. The curves have been obtained using SEVN and the delayed SN model. Line types are the same as in Fig. 4.

3.3 The mass spectrum of compact remnants

In Fig. 6, we show the mass spectrum of compact remnants as a function of the ZAMS mass of their progenitors, for different values of metallicity. To obtain the curves in Fig. 6, we used the delayed SN model, chosen as the default explosion mechanism in SEVN. As expected, in Fig. 6, we notice that the lower the metallicity is, the higher the mass of the heaviest compact remnant; in particular, M_{rem} ranges from $\sim 25 M_{\odot}$ at $Z = 2.0 \times 10^{-2}$ to $\sim 135 M_{\odot}$ at $Z = 1.0 \times 10^{-4}$. For $Z \lesssim 2.0 \times 10^{-4}$ and $7 M_{\odot} = M_{\text{up}} \leq M_{\text{ZAMS}} \leq 150 M_{\odot}$, simple fitting formulas can be derived for $M_{\text{rem}}(M_{\text{ZAMS}})$, by substituting the best-fitting curves for $M_{\text{fin}}(M_{\text{ZAMS}}, Z)$ and $M_{\text{CO}}(M_{\text{ZAMS}}, Z)$ (equations 4 and 5, respectively) in the formulas of the

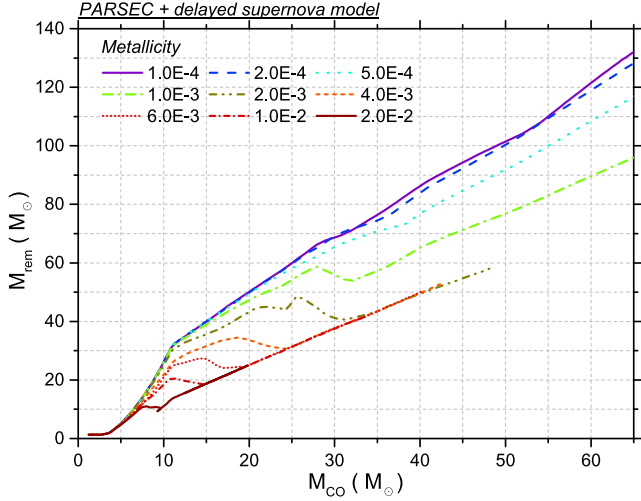


Figure 7. Mass of the compact remnant as a function of the final CO core mass of the progenitor, for different metallicities. The curves have been obtained using SEVN and the delayed SN model. Line types are the same as in Fig. 4.

delayed explosion mechanism (equation B8):

$$M_{\text{rem,bar}} = \begin{cases} 1.4 M_{\odot} & \text{if } M_{\text{up}} \lesssim M_{\text{ZAMS}} \lesssim 13 M_{\odot}, \\ 0.170 M_{\text{ZAMS}} - 0.882 & \text{if } 13 \lesssim M_{\text{ZAMS}}/M_{\odot} \lesssim 16, \\ (0.041 M_{\text{ZAMS}}^3 - 0.673 M_{\text{ZAMS}}^2 + 2.18 M_{\text{ZAMS}} + 0.361) / (0.952 M_{\text{ZAMS}} + 0.15) & \text{if } 16 \lesssim M_{\text{ZAMS}}/M_{\odot} \lesssim 27, \\ (0.0563 M_{\text{ZAMS}}^3 - 1.10 M_{\text{ZAMS}}^2 + 2.49 M_{\text{ZAMS}} + 0.318) / (0.952 M_{\text{ZAMS}} + 0.15) & \text{if } 27 \lesssim M_{\text{ZAMS}}/M_{\odot} \lesssim 36, \\ 0.952 M_{\text{ZAMS}} + 1.45 & \text{if } M_{\text{ZAMS}} \geq 36 M_{\odot}. \end{cases} \quad (6)$$

A general fitting formula for M_{rem} , as a function of M_{ZAMS} and Z , and that holds for every metallicity, is provided in Appendix C.

Fig. 7 shows the value of M_{rem} as a function of M_{CO} , for different metallicities. It is worth noting that, for every metallicity, M_{rem} lies approximately between $M_{\text{rem,up}} = 1.85 M_{\text{CO}} + 11.9$ and $M_{\text{rem,down}} = 1.22 M_{\text{CO}} + 1.06$ (see Appendix C for the details).

3.4 Comparison of different supernova explosion models

In Fig. 8, we show the mass of the remnants as a function of M_{ZAMS} , for different SN recipes, at fixed metallicity $Z = 2.0 \times 10^{-2}$, in order to compare the various SN models implemented in SEVN. In this figure, we also show the results obtained using the SEBA (STARLAB) built-in models (see Portegies Zwart et al. 2001 for details).

Fig. 8 shows that all recipes produce approximately the same remnant mass spectrum, for $M_{\text{ZAMS}} \gtrsim 50 M_{\odot}$. The bottom panel of Fig. 9 is a zoom of Fig. 8 in the region of $25 \leq M_{\text{ZAMS}}/M_{\odot} \leq 50$. From Fig. 9 we notice that the STARTRACK SN recipes produce, on average, more massive BHs (with mass between ~ 12 and $\sim 18 M_{\odot}$) in the interval $28 \lesssim M_{\text{ZAMS}}/M_{\odot} \lesssim 50$. This is due to the fact that

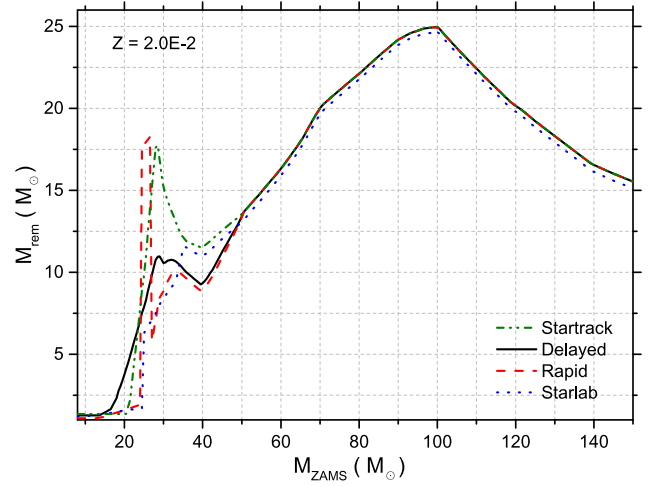


Figure 8. Mass of compact remnants as a function of M_{ZAMS} at $Z = 2.0 \times 10^{-2}$, derived with SEVN using different models of SN explosion. Dash-double dotted line: STARTRACK SN recipes; solid line: delayed SN model; dashed line: rapid SN model; dotted line: STARLAB prescriptions.

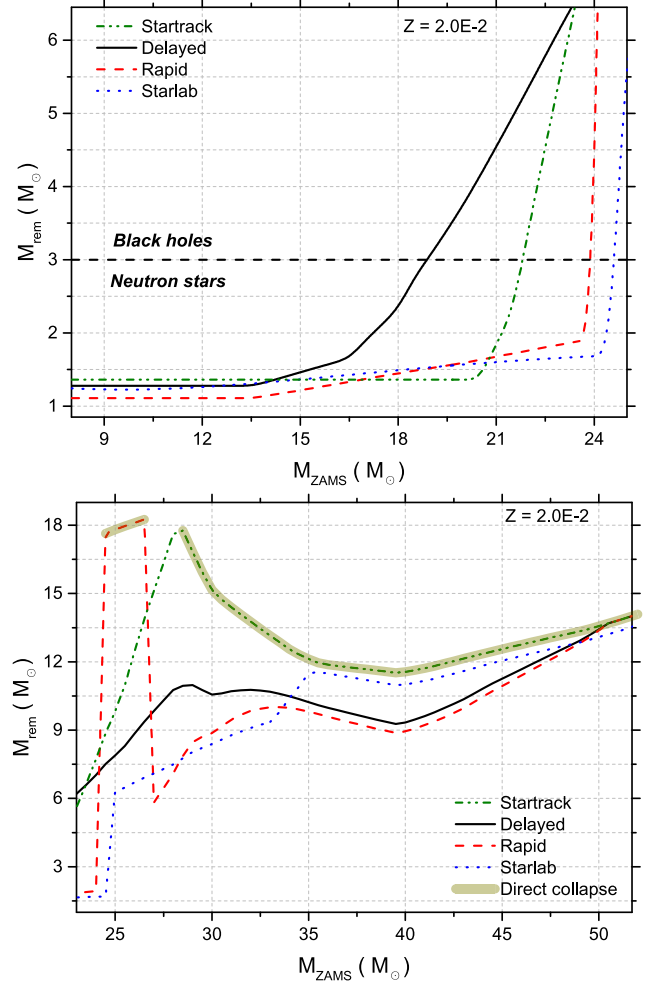


Figure 9. Two details of Fig. 8: the top panel shows the range $8 \lesssim M_{\text{ZAMS}}/M_{\odot} \lesssim 25$, while the bottom panel refers to the interval $25 \lesssim M_{\text{ZAMS}}/M_{\odot} \lesssim 50$. In the top panel, the horizontal dashed line marks the transition between NSs and BHs. The thick, semitransparent line in the bottom panel highlights the intervals in which direct collapse occurs. The other lines are the same as in Fig. 8.

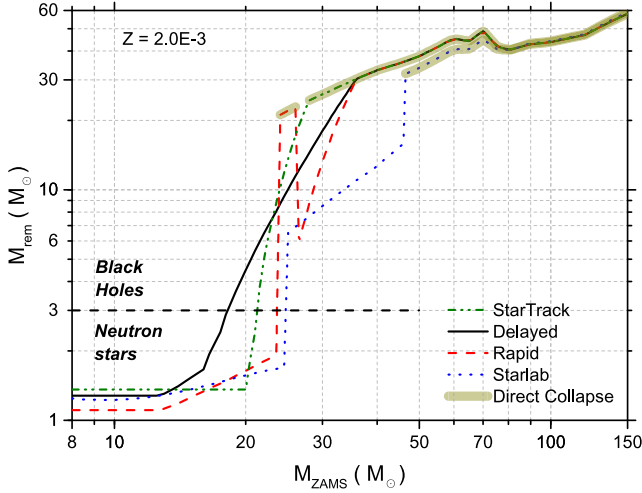


Figure 10. Mass of compact remnants as a function of M_{ZAMS} at $Z = 2.0 \times 10^{-3}$, derived with SEVN using different models of SN explosion. Line types are the same as in Fig. 9.

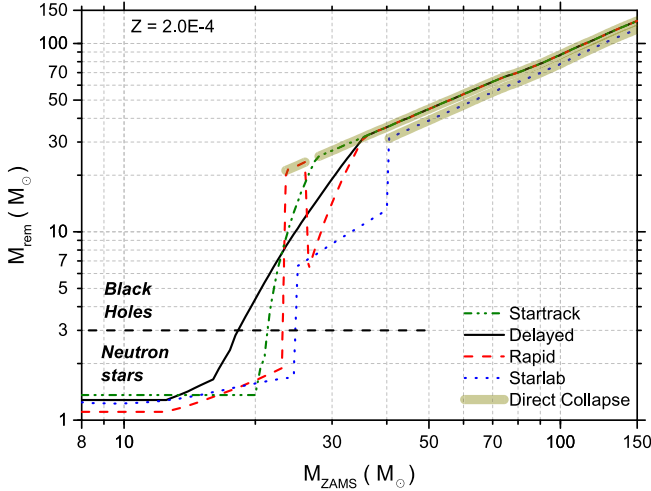


Figure 11. The same as Fig. 10, but for $Z = 2.0 \times 10^{-4}$.

STARTRACK predicts the formation of compact remnants via direct collapse if $M_{\text{CO}} \geq 7.6 M_{\odot}$ (see equation B2), condition that occurs for $M_{\text{ZAMS}} \gtrsim 28 M_{\odot}$ (see Fig. 5). The other models do not predict direct collapse in this interval of M_{ZAMS} , and produce lighter BHs with masses between ~ 6 and $\sim 13 M_{\odot}$.

The abrupt step of the rapid SN model, for $24 \lesssim M_{\text{ZAMS}}/M_{\odot} \lesssim 26$, corresponds to the process of direct collapse that takes place for $6 \leq M_{\text{CO}}/M_{\odot} \leq 7$ in this model (see equation B5).

In the range $14 \leq M_{\text{ZAMS}}/M_{\odot} \leq 24$ (see upper panel of Fig. 9), the delayed model predicts a higher amount of fallback than the other models. In fact, the delayed mechanism forms compact objects with masses between ~ 2.0 and $\sim 6.0 M_{\odot}$, while the other models form remnants with masses only up to $\sim 2 M_{\odot}$ (see upper panel of Fig. 9). Using the STARTRACK prescriptions, it is possible to form remnants with masses $\gtrsim 3.0 M_{\odot}$, but only for $M_{\text{ZAMS}} \gtrsim 22 M_{\odot}$. Finally, using the SN model implemented in SEBA and the rapid SN model, we find a paucity of remnants with masses between ~ 2 and $\sim 6 M_{\odot}$ with the result of having a marked gap between the heaviest NS and the lightest BH.

In Figs 10 and 11, we show the mass spectrum of BHs and NSs obtained for different explosion models for $Z = 2.0 \times 10^{-3}$ and

2.0×10^{-4} , respectively. At $Z = 2.0 \times 10^{-3}$ ($Z = 2.0 \times 10^{-4}$), the maximum BH mass is $\sim 60 M_{\odot}$ ($\sim 130 M_{\odot}$), regardless of the SN explosion mechanism. The main remarkable features of Figs 10 and 11 are the following:

- (i) the STARTRACK models produce heavier compact remnants for $25 \leq M_{\text{ZAMS}}/M_{\odot} \leq 35$;
- (ii) the rapid SN model exhibits an abrupt step for $24 \leq M_{\text{ZAMS}}/M_{\odot} \leq 26$;
- (iii) for $M_{\text{ZAMS}} \gtrsim 35 M_{\odot}$, the mass spectra obtained with the models of Fryer et al. (2012) become indistinguishable (all of them predict direct collapse);
- (iv) except for the delayed model, we obtain a paucity of remnants with masses between ~ 2 and $\sim 6 M_{\odot}$;
- (v) the SEBA built-in SN explosion model predicts direct collapse for $M_{\text{ZAMS}} \gtrsim 45 M_{\odot}$ ($M_{\text{ZAMS}} \gtrsim 40 M_{\odot}$) at $Z = 2.0 \times 10^{-3}$ ($Z = 2.0 \times 10^{-4}$).

In Section 4, we extend this comparison to more sophisticated models of SN explosion (based on the compactness of the stellar core at pre-SN stage, and on the dimensionless entropy per nucleon at pre-SN stage).

3.5 Comparisons with other stellar evolution tools

Fig. 12 shows the mass spectrum of compact remnants, at $Z = 2.0 \times 10^{-2}$, obtained using SEVN, with the delayed supernova explosion model, in comparison with the results of STARLAB v4.4.4 (default SEBA stellar evolution module, hereafter simply STARLAB; Portegies Zwart et al. 2001), STARLABMM (Mapelli et al. 2013) and SSE. The maximum BH mass we obtain, at $Z = 2.0 \times 10^{-2}$, using SEVN, is $\sim 25 M_{\odot}$, while using STARLAB this value is slightly higher ($\sim 28 M_{\odot}$). In SEVN, the stars with $M_{\text{ZAMS}} \simeq 100 M_{\odot}$ form the heaviest BHs, while, using STARLAB, the most massive remnants derive from stars with $85 \leq M_{\text{ZAMS}}/M_{\odot} \leq 150$. STARLABMM produces BHs with masses up to $\sim 23 M_{\odot}$. It is interesting to point out that the recipes implemented in STARLAB produce a paucity of compact remnants with masses between ~ 2 and $\sim 5 M_{\odot}$. This gap derives from

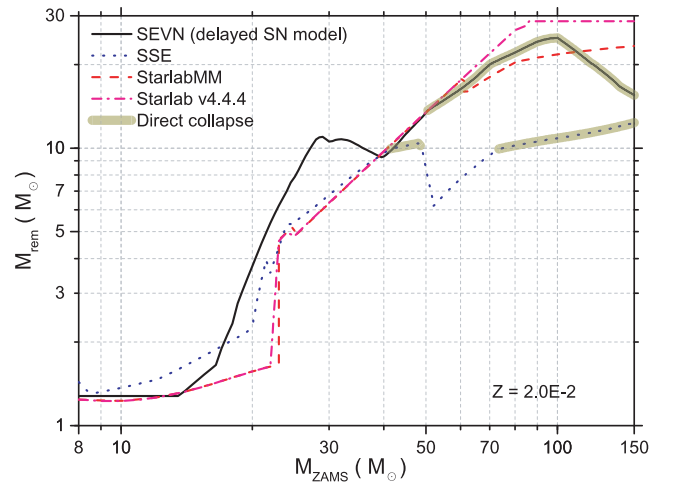


Figure 12. Mass of compact remnants as a function of M_{ZAMS} at $Z = 2.0 \times 10^{-2}$, derived with different codes: SEVN (solid line); SSE (dotted line); STARLABMM (dashed line); STARLAB v4.4.4 (dash-dotted line). The semi-transparent line highlights the intervals in which direct collapse takes place. For SEVN, we used the delayed SN mechanism. STARLABMM is the modified version of STARLAB described in Mapelli et al. (2013), while STARLAB v4.4.4 is the standard version of STARLAB (version 4.4.4).

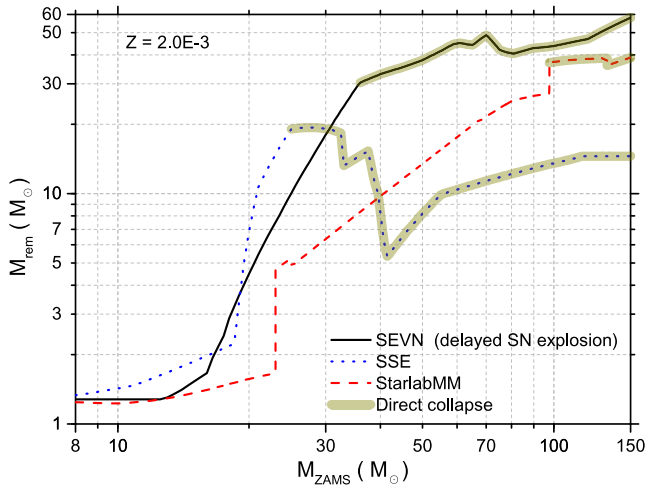


Figure 13. Mass of compact remnants as a function of M_{ZAMS} at $Z = 2.0 \times 10^{-3}$, derived with different codes: SEVN (solid line); SSE (dotted line); STARLABMM (dashed line). The semitransparent line highlights the intervals in which direct collapse takes place. For SEVN, we used the delayed SN mechanism.

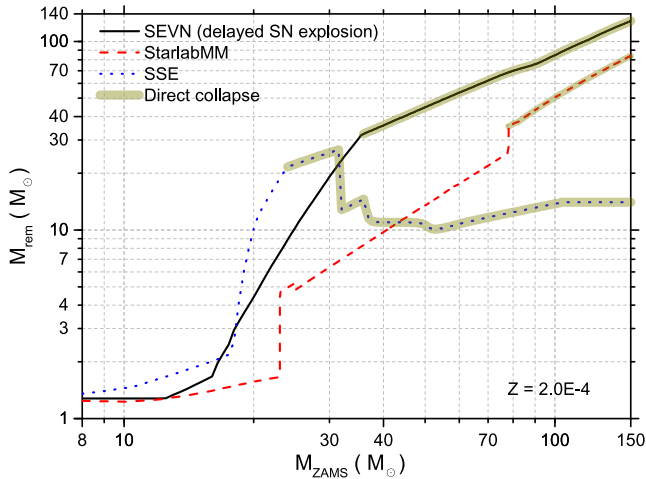


Figure 14. The same as Fig. 13, but for $Z = 2.0 \times 10^{-4}$.

the assumption that BHs form only if $M_{\text{CO}} \geq 5 M_{\odot}$, otherwise, NSs with masses between ~ 1.2 and $\sim 1.6 M_{\odot}$ are formed. If we use the SSE package, the maximum mass of compact remnants is $\sim 13 M_{\odot}$. It is also important to stress that, for $17 \lesssim M_{\text{ZAMS}}/M_{\odot} \lesssim 40$, the delayed explosion model implemented in SEVN creates more massive compact remnants than the other models.

Figs 13 and 14 show the mass spectrum of compact remnants at $Z = 2.0 \times 10^{-3}$ and 2.0×10^{-4} , respectively. The results of STARLAB are not shown in Figs 13 and 14, because STARLAB does not include metallicity-dependent stellar winds. At $Z = 2.0 \times 10^{-3}$ and for $M_{\text{ZAMS}} \gtrsim 30 M_{\odot}$, SEVN (with the PARSEC evolutionary tables) produces significantly heavier BHs than STARLABMM and SSE (see Fig. 13). In particular, the maximum BH mass obtained using SEVN is $\sim 60 M_{\odot}$, while this value is ~ 40 and $\sim 20 M_{\odot}$ in the case of STARLABMM and SSE, respectively. We also stress that, while for SEVN and STARLABMM the heaviest BH comes from the death of the most massive star (that is $M_{\text{ZAMS}} = 150 M_{\odot}$), in the case of SSE BHs of $\sim 20 M_{\odot}$ form from stars with $25 \lesssim M_{\text{ZAMS}}/M_{\odot} \lesssim 30$ only. The abrupt step observed for $M_{\text{ZAMS}} \simeq 100 M_{\odot}$, in the STARLABMM curve represents the transition between partial fallback and direct collapse

Table 1. Values of M_{ZAMS} , M_{fin} and M_{CO} that correspond to the transition between the formation of a NS and that of a BH, and maximum BH mass ($M_{\text{BH}}^{\text{max}}$), for three different codes: SEVN, STARLABMM and SSE. D: delayed model; R: rapid model; S: STARTRACK prescriptions. Results for $Z = 2.0 \times 10^{-2}$.

	SEVN		STARLABMM		SSE
	D	R	S		
$M_{\text{ZAMS}} (M_{\odot})$	18.8	23.9	21.8	23.0	20.7
$M_{\text{fin}} (M_{\odot})$	16.0	19.6	18.7	17.3	7.3
$M_{\text{CO}} (M_{\odot})$	4.1	6.0	5.1	5.0	5.3
$M_{\text{BH}}^{\text{max}} (M_{\odot})$	25.0	25.0	25.0	23.0	12.0

Table 2. Same as Table 1, but for $Z = 2.0 \times 10^{-3}$.

	SEVN		STARLABMM		SSE
	D	R	S		
$M_{\text{ZAMS}} (M_{\odot})$	18.2	23.6	21.3	23.0	18.8
$M_{\text{fin}} (M_{\odot})$	17.9	23.2	21.1	17.6	16.4
$M_{\text{CO}} (M_{\odot})$	4.1	6.0	5.1	5.0	5.1
$M_{\text{BH}}^{\text{max}} (M_{\odot})$	58.0	58.0	58.0	39.0	19.0

Table 3. Same as Table 1, but for $Z = 2.0 \times 10^{-4}$.

	SEVN		STARLABMM		SSE
	D	R	S		
$M_{\text{ZAMS}} (M_{\odot})$	18.2	23.1	21.3	23.0	18.0
$M_{\text{fin}} (M_{\odot})$	18.0	23.1	21.3	17.7	17.0
$M_{\text{CO}} (M_{\odot})$	4.1	6.0	5.1	5.0	5.1
$M_{\text{BH}}^{\text{max}} (M_{\odot})$	130.0	130.0	130.0	83.0	26.0

(occurring at $M_{\text{fin}} \geq 40 M_{\odot}$; see Mapelli et al. 2013 for details), while that at $M_{\text{ZAMS}} \simeq 25 M_{\odot}$ reflects the transition from NSs to BHs. It is worth noting that, for $Z = 2.0 \times 10^{-3}$ and $M_{\text{ZAMS}} \lesssim 30 M_{\odot}$, the SSE model produces more massive compact remnants than the other models.

Similar considerations hold for Fig. 14, which is the same as Figs 12 and 13 but at $Z = 2.0 \times 10^{-4}$. SEVN predicts BHs masses up to $\sim 120 M_{\odot}$, STARLABMM creates BHs of maximum mass $\sim 80 M_{\odot}$, while the SSE prescriptions do not go beyond $\sim 25 M_{\odot}$. Also in this case, as observed at $Z = 2.0 \times 10^{-3}$, the SSE recipes predict the formation of more massive compact remnants in the range $20 \lesssim M_{\text{ZAMS}}/M_{\odot} \lesssim 30$.

Tables 1–3 report the values of M_{ZAMS} , M_{fin} and M_{CO} , corresponding to the transition between the formation of a NS and a BH, at $Z = 2 \times 10^{-2}$, 2×10^{-3} and 2×10^{-4} , respectively. The results obtained using SEVN, STARLABMM and SSE are compared in the tables. We notice that the transition value of M_{CO} does not depend on metallicity and it ranges from $\sim 4.0 M_{\odot}$ (delayed model of SEVN) to $\sim 6.0 M_{\odot}$ (rapid model of SEVN). The transition values of M_{ZAMS} and M_{fin} show a weak dependence on metallicity for a given code. M_{ZAMS} goes from $\sim 18 M_{\odot}$ (delayed model of SEVN at low metallicity) to $\sim 24 M_{\odot}$ (rapid model of SEVN at $Z = 2 \times 10^{-2}$), while M_{fin} ranges from $\sim 7 M_{\odot}$ (SSE at $Z = 2 \times 10^{-2}$) to $23 M_{\odot}$ (rapid model of SEVN at low metallicity). In the last row of Tables 1–3, we also report the maximum compact remnant mass. As we have already shown in this section, for the maximum BH mass we get huge differences between the considered codes. This is due to the different stellar

Table 4. General properties of the stellar populations used as test case to study the mass distribution of NSs and BHs.

Run	Z	SN recipe	Code
Z1D	2×10^{-2}	Delayed SN	SEVN
Z2D	2×10^{-3}	Delayed SN	SEVN
Z3D	2×10^{-4}	Delayed SN	SEVN
Z1R	2×10^{-2}	Rapid SN	SEVN
Z2R	2×10^{-3}	Rapid SN	SEVN
Z3R	2×10^{-4}	Rapid SN	SEVN
Z1S	2×10^{-2}	STARTRACK SN	SEVN
Z2S	2×10^{-3}	STARTRACK SN	SEVN
Z3S	2×10^{-4}	STARTRACK SN	SEVN
Z1MM	2×10^{-2}	Mapelli et al. (2013)	STARLABMM
Z2MM	2×10^{-3}	Mapelli et al. (2013)	STARLABMM
Z3MM	2×10^{-4}	Mapelli et al. (2013)	STARLABMM
Z1SSE	2×10^{-2}	Hurley et al. (2000)	SSE
Z2SSE	2×10^{-3}	Hurley et al. (2000)	SSE
Z3SSE	2×10^{-4}	Hurley et al. (2000)	SSE

Note. We generated and evolved 2.5×10^6 stars in each of these runs.

evolution recipes adopted in PARSEC, SSE and STARLABMM, especially for metal-poor stars.

3.6 The mass distribution of compact remnants

In this section, we derive the mass function of compact remnants (NSs and BHs) that form in a stellar population following the Kroupa initial mass function (IMF; Kroupa 2001). The Kroupa IMF scales as $dN/dm \propto m^{-\alpha}$, with $\alpha = 1.3$ (2.3) for $m < 0.5 M_{\odot}$ ($> 0.5 M_{\odot}$). We assume a minimum mass $m_{\min} = 0.1 M_{\odot}$ and a maximum mass $m_{\max} = 150 M_{\odot}$. We consider three different metallicities ($Z = 2 \times 10^{-2}$, 2×10^{-3} and 2×10^{-4}). For each metallicity, we generate 2.5×10^6 MS stars, with mass distributed according to the Kroupa IMF, and we evolve them with SEVN. For each case, we do three realizations: one with the delayed SN model; one with the rapid SN model and one with the STARTRACK recipes for compact remnants. Moreover, we also compare SEVN (with the delayed SN recipe) with STARLABMM and with SSE. Table 4 lists the properties of the different realizations.

Fig. 15 shows the mass distribution of compact remnants obtained for runs Z1D, Z1R and Z1S (see Table 4). These stellar populations have $Z = 2.0 \times 10^{-2}$ and are evolved using SEVN, with the PARSEC stellar evolution prescriptions and with different SN models (delayed SN model, rapid SN model and STARTRACK recipes for run Z1D, Z1R and Z1S, respectively). Both the delayed and rapid models predict a peak of BHs with mass $\sim 10 M_{\odot}$ at $Z = 2.0 \times 10^{-2}$, while this peak is shifted to $\sim 13 M_{\odot}$ in the STARTRACK prescriptions. The reason for these peaks can be understood from Fig. 9: for example, in the delayed model, BHs of mass $9 \lesssim M_{\text{BH}}/M_{\odot} \lesssim 11$ can form from a wide range of stars (those with $26 \lesssim M_{\text{ZAMS}}/M_{\odot} \lesssim 28$ and with $35 \lesssim M_{\text{ZAMS}}/M_{\odot} \lesssim 44$).

Fig. 15 also shows that the rapid SN model predicts almost no remnants with mass between ~ 2 and $\sim 5 M_{\odot}$. This agrees with current observations, which suggest a gap between the maximum NS mass and the minimum BH mass (Özel et al. 2010).⁹ Figs 16 and 17 are the same as Fig. 15, but for $Z = 2.0 \times 10^{-3}$ (runs Z2D,

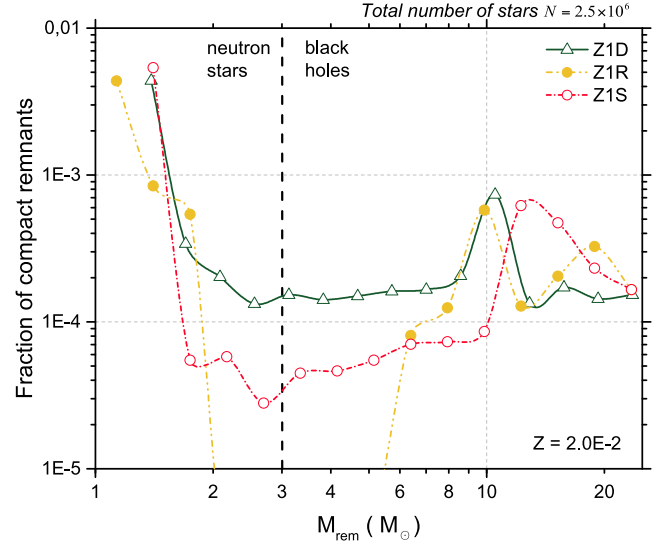


Figure 15. Fraction of compact remnants, normalized to the total number of stars ($N = 2.5 \times 10^6$) that initially follow a Kroupa IMF. Solid line with open triangles: SEVN with delayed SN model (Z1D); dash-double dotted line with circles: SEVN with rapid SN model (Z1R); dash-dotted line with open circles: SEVN with STARTRACK recipes (Z1S). The vertical dashed line at $M_{\text{rem}} = 3 M_{\odot}$ distinguishes NSs from BHs. The curves have been obtained for $Z = 2.0 \times 10^{-2}$.

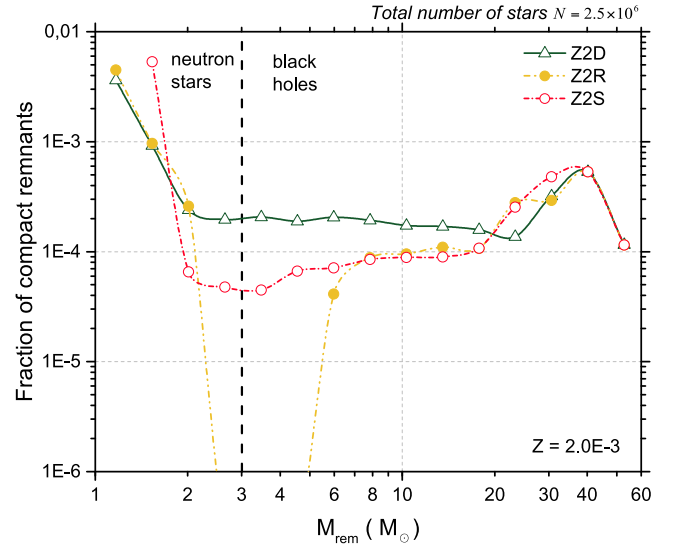


Figure 16. Same as Fig. 15, but for $Z = 2.0 \times 10^{-3}$.

Z2R, Z2S) and $Z = 2.0 \times 10^{-4}$ (runs Z3D, Z3R, Z3S), respectively. In these figures, the peak of BH mass distribution is at ~ 35 – $40 M_{\odot}$.

The mass distribution for NSs peaks at 1.3 – $1.6 M_{\odot}$ for all the SEVN models, almost independently of metallicity. A relevant difference between the models is that the delayed SN model forms a not negligible number of NSs with masses between 2 and $3 M_{\odot}$ while, for the other SN explosion mechanisms, the vast majority of NSs have a mass below $2 M_{\odot}$.

⁹ Whether the presence of this gap is physical or simply due to selection biases is still unclear (Farr et al. 2011; Ugliano et al. 2012; Kochanek 2014), especially after the recent estimation of the BH mass of the X-ray source

SWIFT J1753.5–0127, which seems to fall right into this gap (Neustroev et al. 2014).

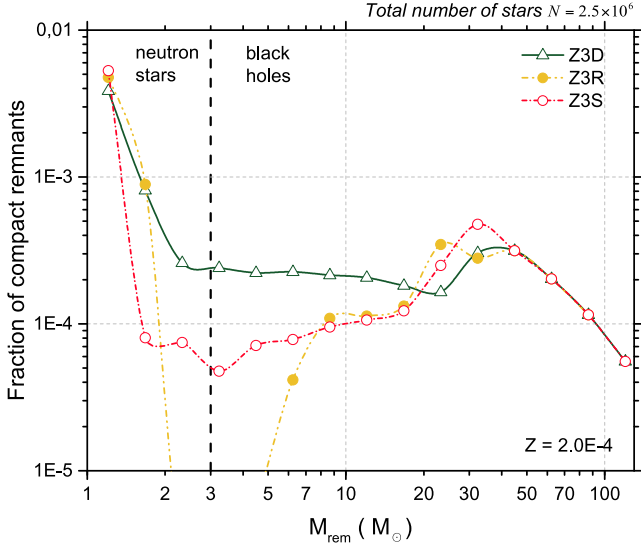
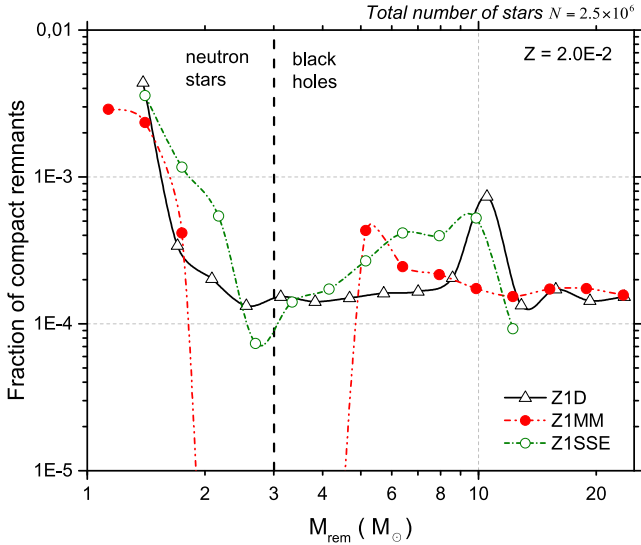
Figure 17. Same as Fig. 15, but for $Z = 2.0 \times 10^{-4}$.

Figure 18. Mass function of NSs and BHs, normalized to the total number of stars ($N = 2.5 \times 10^6$) that initially follow a Kroupa IMF, obtained using three different codes: SEVN; STARLABMM; SSE. Solid line with open triangles: SEVN with the delayed SN model (Z1D); dash-double dotted line with circles: STARLABMM (Z1MM); dash-dotted line with open circles: SSE (Z1SSE). The vertical dashed line at $M_{\text{rem}} = 3 M_{\odot}$ distinguishes NSs from BHs. The curves have been obtained for $Z = 2.0 \times 10^{-2}$.

Fig. 18 compares the mass distribution of compact remnants in runs Z1D, Z1MM and Z1SSE (i.e. the same stellar population at metallicity $Z = 2.0 \times 10^{-2}$, run with SEVN, STARLABMM and SSE, respectively). Run Z1MM (STARLABMM) agrees with run Z1R (SEVN with the rapid SN mechanism) to reproduce the dearth of compact remnants with mass between ~ 2 and $\sim 5 M_{\odot}$. The majority of BHs formed in run Z1SSE (SSE) have mass between ~ 5 and $\sim 12 M_{\odot}$. SSE does not produce compact remnants with mass $\gtrsim 13 M_{\odot}$. As to NSs, SSE produces more NSs with masses between ~ 1.5 and $2.5 M_{\odot}$ than the other codes, while STARLABMM does not form NSs with mass $\gtrsim 1.5 M_{\odot}$.

Figs 19 and 20 are the same as Fig. 18, but for $Z = 2.0 \times 10^{-3}$ and 2.0×10^{-4} , respectively. At low metallicities, SEVN produces

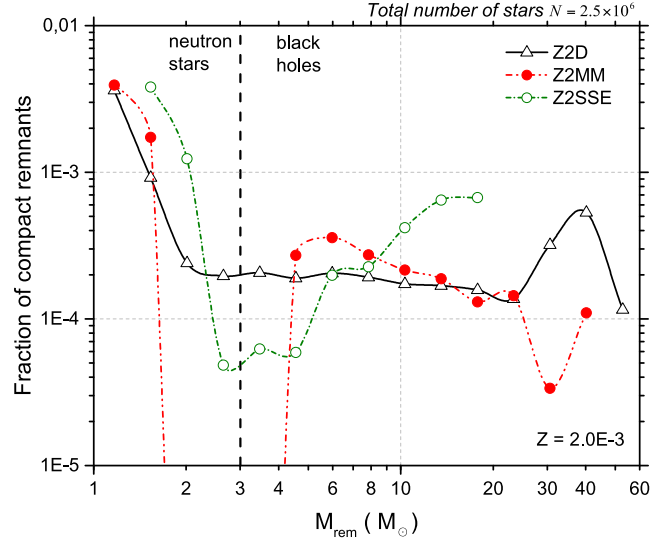
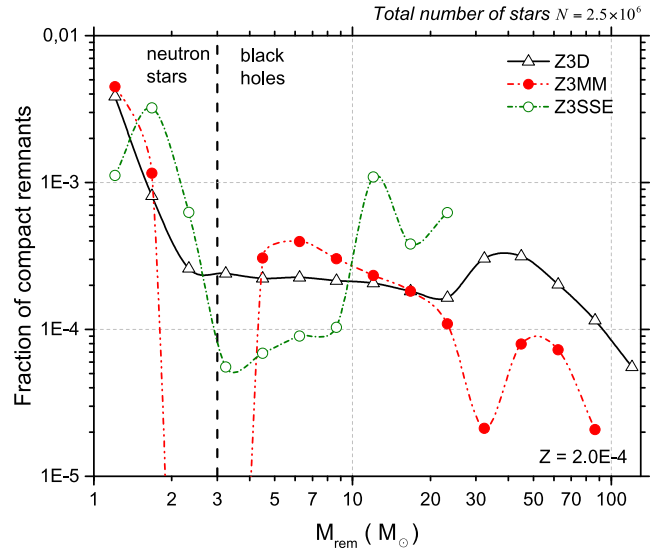
Figure 19. Same as Fig. 18, but for $Z = 2.0 \times 10^{-3}$.Figure 20. Same as Fig. 18, but for $Z = 2.0 \times 10^{-4}$.

Table 5. Fraction of BHs, normalized to total number of stars, obtained from SEVN, adopting different SN explosion models, and from STARLABMM and SSE. D: delayed model; R: rapid model; S: STARTRACK prescriptions.

Z	SEVN			STARLABMM	SSE
	D	R	S		
2.0×10^{-4}	2.38	1.72	1.94	1.72	2.40
2.0×10^{-3}	2.40	1.66	1.92	1.72	2.28
2.0×10^{-2}	2.26	1.62	1.86	1.72	2.02

Note. The values are normalized to 10^{-3} .

heavier BHs than both STARLABMM and SSE. The majority of BHs in both run, Z2SSE and Z3SSE, have mass ~ 10 – $20 M_{\odot}$, while the BH mass in both run, Z2D and Z3D, peaks at about $\sim 40 M_{\odot}$. In run Z2D (run Z3D) the distribution of BH masses extends up to $\sim 60 M_{\odot}$ ($\sim 100 M_{\odot}$). Tables 5 and 6 report the fraction of BHs and massive stellar black holes (MSBHs; i.e. BHs with mass $> 25 M_{\odot}$,

Table 6. Fraction of MSBHs (i.e. BHs with mass $>25 M_{\odot}$), normalized to the total number of stars, obtained from SEVN, adopting different SN explosion models, and from STARLABMM and SSE. D: delayed model; R: rapid model; S: STARTRACK prescriptions.

Z	SEVN			STARLABMM	SSE
	D	R	S		
2.0×10^{-4}	1.04	1.00	1.30	0.20	0.16
2.0×10^{-3}	1.00	0.96	1.24	0.18	0
2.0×10^{-2}	0	0	0	0	0

Note. The values are normalized to 10^{-3} .

according to the definition by Mapelli et al. (2010) that form in our runs.

The fraction of BHs in Table 5 are remarkably similar in all compared codes. Furthermore, this number is almost independent of metallicity. On the other hand, the tested codes exhibit significant differences when the fraction of MSBHs are considered (Table 6). At metallicity $Z = 2.0 \times 10^{-2}$, none of the compared codes forms MSBHs, in agreement with the mass spectra we presented in Fig. 12. At lower metallicity, SEVN produces, on average, five to six times more MSBHs than SSE and STARLABMM. Therefore, the PARSEC stellar evolution prescriptions (combined with Fryer et al. 2012 SN models) tend to form, approximately, the same number of BHs as the other codes, but many more MSBHs at low metallicity.

4 COMPARISON WITH COMPACTNESS-BASED AND TWO-PARAMETER MODELS

The Fryer et al. (2012) SN models we described in Sections 3.3–3.6 (as well as the other explosion prescriptions adopted in N -body simulations so far) are based on a **single-parameter criterion that discriminates between SN explosion and failed SN**. In this framework, stars explode if $M_{\text{CO}} < M_{\text{CO,cut}}$ with $M_{\text{CO,cut}} = 11.0 M_{\odot}$ for the rapid and delayed models and $M_{\text{CO,cut}} = 7.6 M_{\odot}$ for the STARTRACK model. Recent studies have shown that the link between physical properties of the progenitor star, SN properties and mass of the compact remnant is far from being trivial (O’Connor & Ott 2011; Janka 2012; Ugliano et al. 2012; Sukhbold & Woosley 2014; Ertl et al. 2015; Smartt 2015). In particular, it has been shown that the internal structure of the stars at core collapse varies non-monotonically with M_{ZAMS} (or M_{CO}) and this may lead to different compact remnants even if the progenitors had very similar M_{ZAMS} . In this section, we highlight the main differences between criteria based on $M_{\text{CO,cut}}$ and more sophisticated models, based on the structural properties of the star at the pre-SN stage.

4.1 The compactness criterion

O’Connor & Ott (2011) suggest that the value of the compactness ξ_M evaluated just outside the iron core can discriminate between SNe and failed SNe. ξ_M is the ratio between the innermost mass M of the star, in units of M_{\odot} , and the radius $R(M)$ containing M , in units of 1000 km, i.e.

$$\xi_M \equiv \frac{M/M_{\odot}}{R(M)/1000 \text{ km}}. \quad (7)$$

Large values of ξ_M favour failed SNe, while SNe occur for small values of ξ_M . Generally, a fiducial value of $M = 2.5 M_{\odot}$ is used to evaluate the compactness just outside the iron core. Even if the value of $\xi_{2.5}$ is sensible to changes in mass-loss prescriptions and

stellar evolution parameters (such as mixing, reaction rates, opacity, metallicity), a threshold $\xi_{2.5} \sim 0.2$ seems to be a reasonable value to distinguish between the occurrence of explosion and failed SNe (Horiuchi et al. 2011; Smartt 2015). Hereafter, we refer to the $\xi_{2.5}$ -parameter model as ξ -model.

In order to use the ξ -model, SEVN needs further information (in addition to the standard input tables described in Appendix A), that is (i) the value of $R(M)$ at the core collapse stage,¹⁰ to evaluate $\xi_{2.5}$ and to distinguish between SNe and failed SNe; (ii) the mass of the iron core M_{Fe} , which is taken as the mass of the proto-compact object M_{proto} .

Since PARSEC numerically integrates the stellar structure up to the beginning of the CO burning phase only, we merged the PARSEC wind prescriptions with the MESA code (Paxton et al. 2011, 2013) and we used MESA to evolve the PARSEC models until the iron core infall phase. Our grid of MESA simulations goes from $M_{\text{ZAMS}} = 10$ up to $30 M_{\odot}$ with steps of $0.1 M_{\odot}$, and from $M_{\text{ZAMS}} = 30$ to $50 M_{\odot}$ with steps of $0.3 M_{\odot}$.

Fig. 21 shows how the compactness parameter $\xi_{2.5}$ changes as a function of M_{ZAMS} . In this plot, we chose a critical compactness value of $\xi_{2.5} = 0.2$ (Horiuchi et al. 2011, 2014) to separate SNe from failed SNe. The relation between $\xi_{2.5}$ and M_{ZAMS} is quite complex. In particular, with the ξ -model, we distinguish at least three areas:

- (i) range $M_{\text{ZAMS}} \in [10 M_{\odot}; 18 M_{\odot}]$: the majority of stars explode as SN and leave a NS with mass M_{Fe} (excluding fallback material);
- (ii) range $M_{\text{ZAMS}} \in [18 M_{\odot}; 26 M_{\odot}]$: both SNe and failed SNe occur in this mass range;
- (iii) range $M_{\text{ZAMS}} > 26 M_{\odot}$: the majority of stars undergo direct collapse forming a BH with mass $M_{\text{BH}} = M_{\text{fin}}$.

Even if the value of $\xi_{2.5}$ depends on many stellar evolution parameters (including the adopted mass-loss recipes), we find similar results to those obtained by other authors (e.g. Ugliano et al. 2012; Ertl et al. 2015).

4.2 The two-parameter model

A recent study by Ertl et al. (2015) introduces a two-parameter criterion. The two parameters are M_4 , which represents the enclosed mass at a dimensionless entropy per nucleon $s = 4$, and μ_4 , which is the mass gradient at the same location. Following the definition by Ertl et al. (2015), M_4 is normalized to M_{\odot} and μ_4 is normalized to $10^3 \text{ km } M_{\odot}^{-1}$. Ertl et al. (2015) show that a separation curve exists, which divides exploding from non-exploding stars, in the plane $x = M_4 \mu_4$, $y = \mu_4$. The threshold function is a straight line:

$$y_{\text{sep}}(x) = k_1 x + k_2, \quad (8)$$

where the coefficients k_1 and k_2 slightly depend on the different calibrations of the free parameters of Ertl et al. (2015) 1D hydrodynamical simulations. Here, we use the calibration curve for the model w18.0 given by Ertl et al. (2015), for which $k_1 = 0.283$ and $k_2 = 0.043$. Progenitors with $y_{\text{progenitor}} > y_{\text{sep}}$ collapse directly into a BH, otherwise they explode as SN. Hereafter, we refer to this model as 2p-model. In order to apply this criterion to PARSEC progenitors, we extract the values of M_4 and μ_4 from our grid of simulations run with MESA, coupled with the PARSEC wind models (see Section 4.1 for details).

¹⁰ In our models, we identify the pre-SN stage when the collapse speed reaches $\sim 10^8 \text{ cm s}^{-1}$.

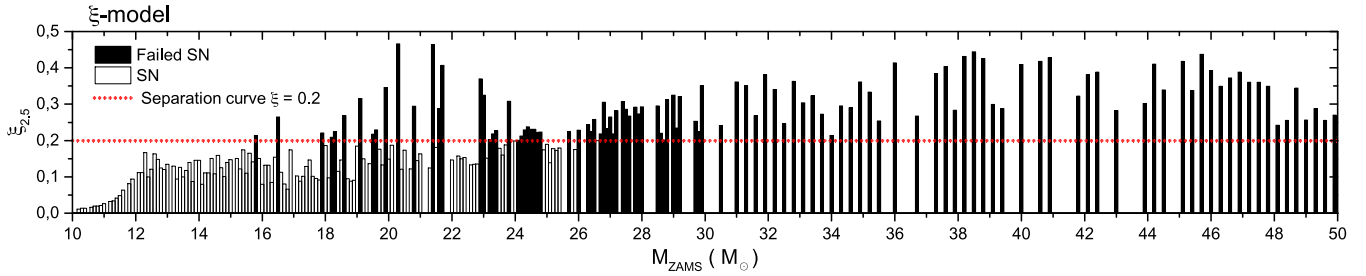


Figure 21. Value of compactness parameter at the innermost $2.5 M_{\odot}$, $\xi_{2.5}$, as a function of M_{ZAMS} , for the PARSEC models evolved until the Fe-core infall using MESA. Black bars indicate non-exploding models (failed SNe) while white bars refer to exploding models (SNe). The dotted line $\xi_{2.5} = 0.2$ is the threshold we chose to distinguish between SNe and failed SNe according to Horiuchi et al. (2014). The simulation grid goes from $M_{ZAMS} = 10.0$ up to $30.0 M_{\odot}$ with steps of $0.1 M_{\odot}$, and from $M_{ZAMS} = 30.0$ to $50.0 M_{\odot}$ with steps of $0.3 M_{\odot}$. Some models in the grid are not shown in the results because of numerical convergence issues.

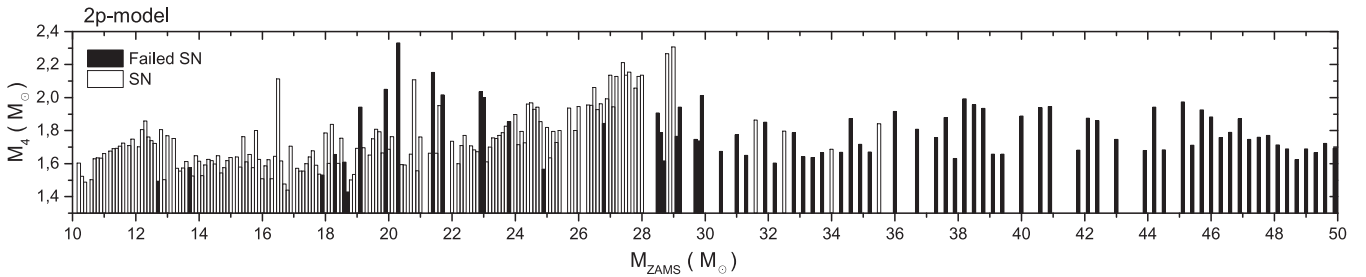


Figure 22. Same as Fig. 21, but here we show the parameter M_4 of the model by Ertl et al. (2015) as a function of M_{ZAMS} . M_4 represents the baryonic mass of the protocompact object following the SN explosion event. In this case, to separate between SNe and failed SNe, we used the linear function $y_{sep}(x) = 0.283x + 0.0430$ which corresponds to the calibration w18.0 of Ertl et al. (2015).

Fig. 22 shows the parameter M_4 (baryonic mass of the remnant if the compact object is a NS) as a function of M_{ZAMS} . Black bars indicate direct collapse while white bars refer to SN explosion events. In this plot, we distinguish four different regions:

- (i) range $M_{ZAMS} \in [10 M_{\odot}; 18 M_{\odot}]$: the majority of stars explode as SNe and leave a NS with baryonic mass M_4 (excluding fallback material);
- (ii) range $M_{ZAMS} \in [18 M_{\odot}; 24 M_{\odot}]$: both SNe and failed SNe occur;
- (iii) range $M_{ZAMS} \in [24 M_{\odot}; 28 M_{\odot}]$: the majority of stars undergo SN explosion;
- (iv) range $M_{ZAMS} > 28 M_{\odot}$: the majority of stars form BHs through direct collapse.

For the calibration we assume, the main difference with the ξ -model (see Fig. 21) is in the range $M_{ZAMS} \in [24 M_{\odot}; 28 M_{\odot}]$, where the 2p-model produces a significantly higher number of NSs. This result confirms that BHs (NSs) can form even for $M_{ZAMS} \lesssim 25 M_{\odot}$ ($M_{ZAMS} \gtrsim 25 M_{\odot}$).

Fig. 23 shows the parameter $y \equiv \mu_4$ as a function of $x \equiv M_4 \mu_4$, for the 2p-model. Filled circles indicate BH formation (via direct collapse) while open triangles refer to the production of NSs (SNe explosion). Our PARSEC progenitors populate a narrow region in the x - y parameter space, whose range is similar to that shown in Ertl et al. (2015).

4.3 Comparison with Fryer et al. (2012) models

Fig. 24 shows the mass spectrum of compact remnants, obtained using the ξ -model (filled circles) and the 2p-model (open triangles), as a function of M_{ZAMS} (black points), at $Z = 0.02$. In the same figure, we also represent the mass spectrum given by the delayed, rapid and

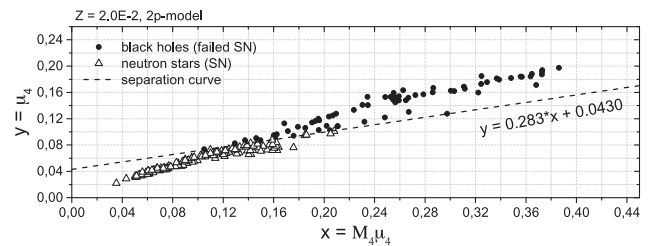


Figure 23. Representation of the results we obtained with PARSEC progenitors in the two-parameter space introduced by Ertl et al. (2015), at $Z = 0.02$. Filled circles represent the formation of BHs via direct collapse, while open triangles refer to SNe. The dashed curve that divides SNe from failed SNe comes from calibration w18.0 of Ertl et al. (2015).

STARTRACK models. Since both the ξ -model and the 2p-model do not provide prescriptions to evaluate the amount of mass that falls back on to the protocompact object, all the models shown in Fig. 24 do not include fallback.

Overall, the mass spectrum of compact remnants resulting from either the ξ -model or the 2p-model is similar to the one derived from the STARTRACK model. The main difference is that the ξ - and 2p-model predict a significant amount of BHs, due to failed SNe, for $M_{ZAMS} < 30 M_{\odot}$. Using the delayed and rapid models, direct collapse occurs for $M_{ZAMS} \gtrsim 50 M_{\odot}$ only.

Finally, Fig. 24 shows that there is a significant mass gap between the heaviest NS ($\sim 2 M_{\odot}$) and the lightest BH ($\sim 12 M_{\odot}$), quite larger than the observed one (Özel et al. 2010; Farr et al. 2011; Ugliano et al. 2012; Kochanek 2014; Neustroev et al. 2014). Still, the area between 2 and $12 M_{\odot}$ may be populated by NSs that accrete

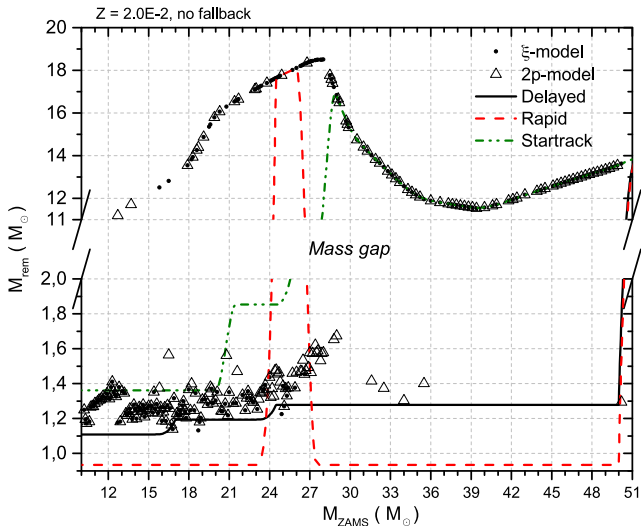


Figure 24. Mass of the compact remnant as a function of M_{ZAMS} for the SN explosion recipes discussed in this paper, at $Z = 0.02$. In particular, filled circles: ξ -model; open triangles: 2p-model; solid line: delayed SN model; long-dashed line: rapid SN model; short-dashed line: STARTRACK recipes. In this plot, fallback is not included. We insert a y-axis break between 2 and $11 M_{\odot}$ to better represent the mass spectrum of both BHs and NSs for the various models and the mass gap between the heaviest NS and the lightest BH.

mass through the fallback mechanism,¹¹ and/or by NSs that accrete mass from a companion, in a binary system.

5 CONCLUSIONS

The mass spectrum of BHs is still an open issue: only a few dynamical mass measurements of BHs are available (Özel et al. 2010), while theoretical models are affected by the uncertainties on SN explosion and massive star evolution. In this paper, we derive the mass spectrum of compact remnants based on the new stellar evolution models implemented in PARSEC (Bressan et al. 2012; Chen et al. 2014; Tang et al. 2014), combined with different recipes for SN explosion: the rapid and delayed SN models presented in Fryer et al. (2012), the SN model implemented in the STARTRACK code (Belczynski et al. 2008), the SN recipes included in STARLAB through the SEBA module (Portegies Zwart et al. 2001), and (for $Z = 0.02$) the ξ - and the 2p-model (O’Connor & Ott 2011; Ertl et al. 2015).

These recipes for stellar evolution and SN explosion are implemented in our new public tool SEVN, which can be used both as a stand-alone population synthesis code or as a module in several N -body codes (STARLAB, HIGPUS). SEVN is extremely versatile, because it calculates the mass, radius, luminosity, temperature and chemical evolution of a star based on stellar evolution tables. We adopt stellar evolution tables that have been generated with the PARSEC code, but these can be substituted with different stellar evolution models in a fast and simple way.

With respect to previous stellar evolution codes, PARSEC predicts significantly larger values of M_{fin} and M_{CO} at low metallicity ($\lesssim 2 \times 10^{-3}$, Figs 4 and 5). We find differences up to ~ 80 per cent

between the value of M_{fin} calculated by PARSEC and the fitting formulas implemented in SSE (Fig. 3). This implies that SEVN predicts substantially larger BH masses at low metallicity, since the mass of the compact remnants depends on M_{fin} and M_{CO} in the SN models developed by Fryer et al. (2012).

Moreover, for a metallicity $Z = 0.02$ and for $M_{\text{ZAMS}} \leq 50 M_{\odot}$, we also present the mass spectrum of NSs and BHs given by the ξ -model (O’Connor & Ott 2011) and the 2p-model (Ertl et al. 2015). These models depend on stellar structural parameters evaluated at the time of iron core infall. Coupling these new prescriptions with the PARSEC stellar models, we find that the relation between progenitor mass and remnant mass is quite complex, especially in the range $M_{\text{ZAMS}} \in [18 M_{\odot}; 30 M_{\odot}]$ (see Figs 21 and 22). A detailed study that considers also $Z \neq 0.02$ and $M_{\text{ZAMS}} > 50 M_{\odot}$ is still in progress.

Using the Fryer et al. (2012) models, we find that the maximum BH mass found with SEVN is ~ 25 , 60 and $130 M_{\odot}$ at $Z = 2 \times 10^{-2}$, 2×10^{-3} and 2×10^{-4} , respectively. Mass loss by stellar winds plays a major role in determining the mass of BHs for very massive stars ($\gtrsim 90 M_{\odot}$), almost independently of the adopted SN recipe. In contrast, the adopted SN model is very important for lower BH masses, and for the transition between NSs and BHs (Figs 8–11): according to the delayed SN model, stars with $M_{\text{ZAMS}} > 19 M_{\odot}$ end their life as BHs, while this limit is $M_{\text{ZAMS}} > 24$ – $25 M_{\odot}$ if the rapid SN mechanism or the SEBA recipes are assumed.

As a consequence, the rapid SN mechanism and the recipes implemented in SEBA predict a gap between the maximum mass of NSs and the minimum mass of BHs, while the delayed SN model (and the STARTRACK recipes) suggests a smooth transition between NSs and BHs (Figs 15–17). The distribution of dynamically measured BH and NS masses in the local Universe suggests the existence of a gap between NS and BH masses (Özel et al. 2010), even if the statistical significance of this result is still debated (Farr et al. 2011; Ugliano et al. 2012; Kochanek 2014; Neustroev et al. 2014).

According to SEVN (with either the delayed or the rapid SN model), at $Z = 2 \times 10^{-2}$ most BHs have mass 8–12 M_{\odot} , while at $2 \times 10^{-3} \geq Z \geq 2 \times 10^{-4}$ most BHs have mass 20–60 M_{\odot} (Figs 15–17).

For a stellar population following the Kroupa IMF, the total number of BHs predicted by SEVN in its various SN flavours is remarkably similar to other codes, such as STARLABMM (Mapelli et al. 2013) and SSE (Hurley et al. 2000). Furthermore, the fraction of BHs are almost independent of metallicity. On the other hand, the fraction of MSBHs (i.e. BHs with mass $> 25 M_{\odot}$) strongly depend on the metallicity and on the assumed stellar evolution recipes. At metallicity $Z = 2.0 \times 10^{-2}$, no MSBHs form from single-star evolution, using either SEVN or STARLABMM or SSE. At lower metallicity, SEVN produces, on average, five to six times more MSBHs than SSE and STARLABMM.

This might have dramatic consequences for both the number of X-ray binaries powered by MSBHs and the detection of gravitational waves by BH–BH binary mergers. As to X-ray binaries, models by Mapelli & Zampieri (2014), based on STARLABMM, indicate that MSBHs are expected to power ~ 20 per cent of the Roche lobe overflow BH binaries in a young star cluster with $Z \lesssim 2 \times 10^{-3}$. With the recipes implemented in SEVN, the fraction of X-ray binaries powered by MSBHs might be substantially higher. On the other hand, quantifying the difference with previous studies is non-trivial, because the evolution of binary systems and dynamical encounters in star clusters can significantly affect the demographics of BH binaries. In a forthcoming study, we will use SEVN to investigate

¹¹ Ertl et al. (2015) show that a typical amount of mass that falls back on to the protocompact object is $\sim 0.05 M_{\odot}$. Values larger than $1 M_{\odot}$ are rare (only six events over ~ 600 progenitor models).

the demographics of X-ray binaries and BH–BH binaries in star clusters.

ACKNOWLEDGEMENTS

We thank the anonymous referee for suggestions that helped us to improve the paper. MM and MS acknowledge financial support from the Italian Ministry of Education, University and Research (MIUR) through grant FIRB 2012 RBFR12PM1F. The authors acknowledge financial support from INAF through grant PRIN-2014-14.

REFERENCES

- Aarseth S. J., 1999, *PASP*, 111, 1333
- Belczynski K., Kalogera V., Bulik T., 2002, *ApJ*, 572, 407
- Belczynski K., Kalogera V., Rasio F. A., Taam R. E., Zezas A., Bulik T., Maccarone T. J., Ivanova N., 2008, *ApJS*, 174, 223
- Belczynski K., Bulik T., Fryer C. L., Ruiter A., Valsecchi F., Vink J. S., Hurley J. R., 2010, *ApJ*, 714, 1217
- Bethe H. A., 1990, *Rev. Modern Phys.*, 62, 801
- Blecha L., Ivanova N., Kalogera V., Belczynski K., Fregeau J., Rasio F., 2006, *ApJ*, 642, 427
- Böhm-Vitense E., 1958, *Z. Astrophys.*, 46, 108
- Bressan A. G., Chiosi C., Bertelli G., 1981, *A&A*, 102, 25
- Bressan A., Marigo P., Girardi L., Salasnich B., Dal Cero C., Rubele S., Nanni A., 2012, *MNRAS*, 427, 127
- Bressan A., Marigo P., Girardi L., Nanni A., Rubele S., 2013, *European Phys. J. Web Conf.*, 43, 3001
- Burrows A., 2013, *Rev. Modern Phys.*, 85, 245
- Caffau E., Ludwig H.-G., Steffen M., Freytag B., Bonifacio P., 2011, *Sol. Phys.*, 268, 255
- Capuzzo-Dolcetta R., Spera M., Punzo D., 2013, *J. Comput. Phys.*, 236, 580
- Chen Y., Girardi L., Bressan A., Marigo P., Barbieri M., Kong X., 2014, *MNRAS*, 444, 2525
- Clausen D., Piro A. L., Ott C. D., 2015, *ApJ*, 799, 190
- Crowther P. A., Carpano S., Hadfield L. J., Pollock A. M. T., 2007, *A&A*, 469, L31
- Crowther P. A., Barnard R., Carpano S., Clark J. S., Dhillon V. S., Pollock A. M. T., 2010, *MNRAS*, 403, L41
- Cyburt R. H. et al., 2010, *ApJS*, 189, 240
- Dehevels S. et al., 2010, *A&A*, 514, A31
- de Jager C., Nieuwenhuijzen H., van der Hucht K. A., 1988, *A&AS*, 72, 259
- Dewitt H. E., Graboske H. C., Cooper M. S., 1973, *ApJ*, 181, 439
- Downing J. M. B., 2012, *MNRAS*, 425, 2234
- Downing J. M. B., Benacquista M. J., Giersz M., Spurzem R., 2010, *MNRAS*, 407, 1946
- Downing J. M. B., Benacquista M. J., Giersz M., Spurzem R., 2011, *MNRAS*, 416, 133
- Ertl T., Janka H.-T., Woosley S. E., Sukhbold T., Ugliano M., 2015, *ApJ*, preprint ([arXiv:1503.07522](https://arxiv.org/abs/1503.07522))
- Farr W. M., Sravan N., Cantrell A., Kreidberg L., Bailyn C. D., Mandel I., Kalogera V., 2011, *ApJ*, 741, 103
- Fryer C. L., 1999, *ApJ*, 522, 413
- Fryer C. L., 2006, *New Astron. Rev.*, 50, 492
- Fryer C. L., Kalogera V., 2001, *ApJ*, 554, 548
- Fryer C. L., Belczynski K., Wiktorowicz G., Dominik M., Kalogera V., Holz D. E., 2012, *ApJ*, 749, 91
- Garnett D. R., 1990, *ApJ*, 363, 142
- Gerke J. R., Kochanek C. S., Stanek K. Z., 2015, *MNRAS*, 450, 3289
- Girardi L., Rubele S., Kerber L., 2009, *MNRAS*, 394, L74
- Graboske H. C., Dewitt H. E., Grossman A. S., Cooper M. S., 1973, *ApJ*, 181, 457
- Gräfener G., Hamann W.-R., 2008, *A&A*, 482, 945
- Grevesse N., Sauval A. J., 1998, *Space Sci. Rev.*, 85, 161
- Haft M., Raffelt G., Weiss A., 1994, *ApJ*, 425, 222
- Heger A., Woosley S. E., 2002, *ApJ*, 567, 532
- Heger A., Fryer C. L., Woosley S. E., Langer N., Hartmann D. H., 2003, *ApJ*, 591, 288
- Hobbs G., Lorimer D. R., Lyne A. G., Kramer M., 2005, *MNRAS*, 360, 974
- Horiuchi S., Beacom J. F., Kochanek C. S., Prieto J. L., Stanek K. Z., Thompson T. A., 2011, *ApJ*, 738, 154
- Horiuchi S., Nakamura K., Takiwaki T., Kotake K., Tanaka M., 2014, *MNRAS*, 445, L99
- Humphreys R. M., Davidson K., 1979, *ApJ*, 232, 409
- Hurley J. R., Pols O. R., Tout C. A., 2000, *MNRAS*, 315, 543
- Iglesias C. A., Rogers F. J., 1996, *ApJ*, 464, 943
- Itoh N., Kohyama Y., 1983, *ApJ*, 275, 858
- Itoh N., Uchida S., Sakamoto Y., Kohyama Y., Nozawa S., 2008, *ApJ*, 677, 495
- Janka H.-T., 2012, *Annu. Rev. Nucl. Part. Sci.*, 62, 407
- Janka H.-T., Langanke K., Marek A., Martínez-Pinedo G., Müller B., 2007, *Phys. Rep.*, 442, 38
- Jennings Z. G., Williams B. F., Murphy J. W., Dalcanton J. J., Gilbert K. M., Dolphin A. E., Foesneau M., Weisz D. R., 2012, *ApJ*, 761, 26
- Jennings Z. G., Williams B. F., Murphy J. W., Dalcanton J. J., Gilbert K. M., Dolphin A. E., Weisz D. R., Foesneau M., 2014, *ApJ*, 795, 170
- Justham S., Schawinski K., 2012, *MNRAS*, 423, 1641
- Kamath D., Wood P. R., Soszyński I., Lebzelter T., 2010, *MNRAS*, 408, 522
- Kochanek C. S., 2014, *ApJ*, 785, 28
- Kroupa P., 2001, *MNRAS*, 322, 231
- Kudritzki R. P., 2002, *ApJ*, 577, 389
- Kudritzki R.-P., Puls J., 2000, *ARA&A*, 38, 613
- Kudritzki R. P., Pauldrach A., Puls J., 1987, *A&A*, 173, 293
- Lattimer J. M., 2012, *Annu. Rev. Nucl. Part. Sci.*, 62, 485
- Lattimer J. M., Prakash M., 2005, *Phys. Rev. Lett.*, 94, 111101
- Leitherer C., Robert C., Drissen L., 1992, *ApJ*, 401, 596
- Mapelli M., Bressan A., 2013, *MNRAS*, 430, 3120
- Mapelli M., Zampieri L., 2014, *ApJ*, 794, 7
- Mapelli M., Colpi M., Zampieri L., 2009, *MNRAS*, 395, L71
- Mapelli M., Ripamonti E., Zampieri L., Colpi M., Bressan A., 2010, *MNRAS*, 408, 234
- Mapelli M., Zampieri L., Ripamonti E., Bressan A., 2013, *MNRAS*, 429, 2298
- Marigo P., Aringer B., 2009, *A&A*, 508, 1539
- Marigo P., Bressan A., Nanni A., Girardi L., Pumo M. L., 2013, *MNRAS*, 434, 488
- Meynet G., Maeder A., 2005, *A&A*, 429, 581
- Miller M. C., Hamilton D. P., 2002, *MNRAS*, 330, 232
- Munakata H., Kohyama Y., Itoh N., 1985, *ApJ*, 296, 197
- Neustroev V. V., Veledina A., Poutanen J., Zharikov S. V., Tsygankov S. S., Sjöberg G., Kajava J. J. E., 2014, *MNRAS*, 445, 2424
- Nitadori K., Aarseth S. J., 2012, *MNRAS*, 424, 545
- Nugis T., Lamers H. J. G. L. M., 2000, *A&A*, 360, 227
- O'Connor E., Ott C. D., 2011, *ApJ*, 730, 70
- O'Leary R. M., Rasio F. A., Fregeau J. M., Ivanova N., O'Shaughnessy R., 2006, *ApJ*, 637, 937
- Oppenheimer J. R., Volkoff G. M., 1939, *Phys. Rev.*, 55, 374
- Orosz J. A. et al., 2007, *Nature*, 449, 872
- Özel F., Psaltis D., Narayan R., McClintock J. E., 2010, *ApJ*, 725, 1918
- Paczynski B., 1991, *Acta Astron.*, 41, 257
- Paxton B., Bildsten L., Dotter A., Herwig F., Lesaffre P., Timmes F., 2011, *ApJS*, 192, 3
- Paxton B. et al., 2013, *ApJS*, 208, 4
- Pejcha O., Prieto J. L., 2015, *ApJ*, preprint ([arXiv:1501.06573](https://arxiv.org/abs/1501.06573))
- Pelupessy F. I., van Elteren A., de Vries N., McMillan S. L. W., Drost N., Portegies Zwart S. F., 2013, *A&A*, 557, A84
- Phinney E. S., 1991, *ApJ*, 380, L17
- Pilyugin L. S., Vílchez J. M., Contini T., 2004, *A&A*, 425, 849
- Portegies Zwart S. F., McMillan S. L. W., 2002, *ApJ*, 576, 899
- Portegies Zwart S. F., McMillan S. L. W., Hut P., Makino J., 2001, *MNRAS*, 321, 199
- Prestwich A. H. et al., 2007, *ApJ*, 669, L21
- Rosenfield P. et al., 2014, *ApJ*, 790, 22

- Sadowski A., Belczynski K., Bulik T., Ivanova N., Rasio F. A., O'Shaughnessy R., 2008, *ApJ*, 676, 1162
- Silverman J. M., Filippenko A. V., 2008, *ApJ*, 678, L17
- Sippel A. C., Hurley J. R., Madrid J. P., Harris W. E., 2012, *MNRAS*, 427, 167
- Smartt S. J., 2009, *ARA&A*, 47, 63
- Smartt S. J., 2015, *Publ. Astron. Soc. Aust.*, 32, e016
- Sukhbold T., Woosley S. E., 2014, *ApJ*, 783, 10
- Tang J., Bressan A., Rosenfield P., Slemmer A., Marigo P., Girardi L., Bianchi L., 2014, *MNRAS*, 445, 4287
- Timmes F. X., Woosley S. E., Weaver T. A., 1996, *ApJ*, 457, 834
- Torres G., Vaz L. P. R., Sandberg Lacy C. H., Claret A., 2014, *AJ*, 147, 36
- Trani A. A., Mapelli M., Bressan A., 2014, *MNRAS*, 445, 1967
- Ugliano M., Janka H.-T., Marek A., Arcones A., 2012, *ApJ*, 757, 69
- Vink J. S., de Koter A., 2005, *A&A*, 442, 587
- Vink J. S., de Koter A., Lamers H. J. G. L. M., 2000, *A&A*, 362, 295
- Vink J. S., de Koter A., Lamers H. J. G. L. M., 2001, *A&A*, 369, 574
- Vink J. S., Muijres L. E., Anthonisse B., de Koter A., Gräfenr G., Langer N., 2011, *A&A*, 531, A132
- Woosley S. E., Heger A., Weaver T. A., 2002, *Rev. Modern Phys.*, 74, 1015
- Ziosi B. M., Mapelli M., Branchesi M., Tormen G., 2014, *MNRAS*, 441, 3703

APPENDIX A: NOTES ON THE IMPLEMENTATION OF SEVN

A1 General scheme

As we discussed in Section 2.2, *SEVN* can be used as a stand-alone population synthesis code and/or can be easily linked to several *N*-body codes. It is extremely versatile because it relies upon a set of isochrones as input files; this means that we can easily change stellar evolution recipes by simply substituting the input tables.

SEVN reads a single file that contains a set of isochrones, which are provided by a stellar evolution code (by *PARSEC*, in the current version of *SEVN*). By default, the name of this file must have the form *TABLEZN.DAT*, where *N* indicates the metallicity *Z*. Inside this file, the isochrones are separated by a line reporting the age (in Gyr), and the number of points of the following isochrone. Each isochrone is composed of nine columns that indicate (1) the initial mass of the star, (2) its present mass, (3) the logarithm of luminosity, (4) the effective temperature, (5) the logarithm of radius, (6) the logarithm of surface gravity, (7) the helium core mass, (8) the carbon–oxygen core mass and (9) the stellar type at the current age. All given values are in solar units, except for the effective temperature, which is absolute and expressed in Kelvin. We stress that the isochrones do not need to be equally spaced in mass or other quantities.

In order to speed up the calculations, *SEVN* reads the isochrone file and rearranges it in a more convenient way. First of all, an equally spaced grid of masses is chosen.¹² For each star in the grid, we construct the time evolution of its physical parameters, recording information whenever the value of a generic stellar parameter is varied by more than 5 per cent. The result is stored in seven different files containing the time evolution of masses, radii, luminosities, stellar phases, carbon–Oxygen core mass, helium core mass and the corresponding ages when the stellar parameters need to be updated.

These seven files are then loaded in a three-dimensional structure where the first index (line number, *L*) identifies the initial mass of the star. The second index (column number, *C*) gives information about the current stellar age, and the third index, *P*, refers to the specific stellar parameter we need to read or write. Thus, *L* ranges

between 1 and the number of points of the grid of masses, $1 \leq P \leq 7$, and *C* varies from 1 to the number of update points needed for a generic star.

At the beginning of the integration, it is possible to associate two different mass indexes, *L*₁ and *L*₂, to each star in order to uniquely identify its position in the grid. For example, let us consider a grid of masses that goes from 0.1 to 150 *M*_⊙ with steps of 0.5 *M*_⊙. The evolution of a star *S* of mass *M*_s = 50.3 *M*_⊙ will be derived interpolating the evolutionary tracks of the nearest neighbour stars, that is *M*₁ = 50 *M*_⊙ and *M*₂ = 50.5 *M*_⊙, and we can compute the stellar parameters of the star *S* using the weights

$$\alpha_1 = \frac{M_2 - M_s}{(M_s - M_1) + (M_2 - M_s)},$$

$$\alpha_2 = \frac{M_s - M_1}{(M_s - M_1) + (M_2 - M_s)}. \quad (\text{A1})$$

To evolve the parameters of a generic star, we use linear interpolations. Let us consider again a test star *S* with initial mass *M*_s(*t* = 0) = 50.3 *M*_⊙. At time *t* = *t*₁, this star will have a mass *M*_s(*t*₁). In order to evolve the star at time *t*₂ = *t*₁ + Δ*t*, we need to use the information of its neighbour grid stars of mass *M*₁(0) = 50 *M*_⊙ and *M*₂(0) = 50.5 *M*_⊙. First of all, the code must compute the quantities *M*₁(*t*₂) and *M*₂(*t*₂). In general, a generic time *t*₂ will not be included in the tables. Thus, *SEVN* reads the tables and searches the values *M*₁(*t*₃), *M*₁(*t*₄), *M*₂(*t*₅) and *M*₂(*t*₆) such that *t*₃ ≲ *t*₂ ≲ *t*₄ and *t*₅ ≲ *t*₂ ≲ *t*₆. The code then calculates *M*₁(*t*₂) and *M*₂(*t*₂) with a linear interpolation:

$$M_1(t_2) = m_1 t_2 + q_1,$$

$$M_2(t_2) = m_2 t_2 + q_2, \quad (\text{A2})$$

where

$$m_1 = \frac{M_1(t_4) - M_1(t_3)}{t_4 - t_3},$$

$$m_2 = \frac{M_2(t_6) - M_2(t_5)}{t_6 - t_5},$$

$$q_1 = M_1(t_4) - m_1 t_4,$$

$$q_2 = M_2(t_6) - m_2 t_6. \quad (\text{A3})$$

Finally, the value *M*_s(*t*₂) is derived with a further linear interpolation, that is

$$M_s(t_2) = \alpha_1 M_1(t_2) + \alpha_2 M_2(t_2), \quad (\text{A4})$$

with weights α_1 and α_2 given in equation (A1). The same procedure is adopted to obtain the other stellar parameters needed at a given age.

A2 Integration of SEVN in STARLAB

As discussed in Section 2.2, we have merged *SEVN* with the *STARLAB* software environment (Portegies Zwart et al. 2001), and with the direct *N*-body code *HIGPUS* (Capuzzo-Dolcetta et al. 2013; Spera, in preparation). In order to combine *SEVN* with *STARLAB*, we modified the *SEBA* stellar evolution module. In particular, *SEBA* is a C++ module based on a structure of classes, in which each class approximately corresponds to a stellar evolution phase. In order to easily match the *SEBA* internal organization and the implemented transitions between stellar evolution phases, we identify the main stellar evolution phases using integer indexes. Namely,

¹² By default, the grid goes from 0.1 to 150 *M*_⊙ with steps of 0.5 *M*_⊙.

- (i) 0 identifies pre-MS and MS stars that are mapped to the SEBA class MAIN_SEQUENCE;
- (ii) 1 indicates stars in the subgiant phase; in this case, we have a one-to-one correspondence with the SUB_GIANT class;
- (iii) 2 groups several categories of stars (among which red giants, blue and red supergiants, LBVs and WRs) in the HYPER_GIANT class;
- (iv) 3 refers to core helium burning stars, collected in the HORIZONTAL_BRANCH class;
- (v) 4 corresponds to stars in the early asymptotic giant branch (E-AGB) phase, mapped to the HYPER_GIANT class.

Using our simplified scheme, we lose information about some specific characteristics of the stars during the numerical integration; for instance, we do not know if a star is a WR, a LBV or a blue supergiant or a red supergiant. Anyway, all these features can be recovered a posteriori by the ages, radii, luminosities and temperatures printed in the output files.

During the pre-MS and MS phases we evolve mass, luminosity and radius of the stars following our input tables by means of linear interpolations in time and mass. Stellar evolution continues until the function CREATE_REMNANT() is called. This routine contains our updated recipes for SN explosion, and converts the star into a compact remnant, which can be either a WD, a NS or a BH, depending on the final state of the star.

At present, since PARSEC does not include evolutionary prescriptions for stars that undergo the TP-AGB phase, we use the SEBA built-in class SUPER_GIANT to follow their evolution through this stage (see Portegies Zwart et al. 2001 for the details). In particular, we assume that the stars that undergo the TP-AGB phase are those with $M_{ZAMS} \lesssim M_{up} = 7 M_{\odot}$.

APPENDIX B: SN EXPLOSION MECHANISMS IN SEVN

Here we summarize the main features of the Fryer et al. (2012) recipes.

B1 STARTRACK model

In the case of STARTRACK recipes, stars form a protocompact object of mass M_{proto} given by

$$M_{proto} = \begin{cases} 1.50 M_{\odot} & M_{CO} < 4.82 M_{\odot}, \\ 2.11 M_{\odot} & 4.82 \leq M_{CO}/M_{\odot} < 6.31, \\ 0.69 M_{CO} - 2.26 M_{\odot} & 6.31 \leq M_{CO}/M_{\odot} < 6.75, \\ 0.37 M_{CO} - 0.07 M_{\odot} & M_{CO} \geq 6.75 M_{\odot}. \end{cases} \quad (B1)$$

f_{fb} is the *fractional fallback parameter*, and is such that $M_{fb} = f_{fb}(M_{fin} - M_{proto})$, where M_{fin} is the final mass of the star. According to STARTRACK prescriptions, the values of f_{fb} are the following:

$$f_{fb} = \begin{cases} 0 & M_{CO} < 5.0 M_{\odot}, \\ 0.378 M_{CO} - 1.889 & 5.0 \leq M_{CO}/M_{\odot} < 7.6, \\ 1.0 & M_{CO} \geq 7.6 M_{\odot}. \end{cases} \quad (B2)$$

From the baryonic mass of the remnant $M_{rem,bar} = M_{proto} + M_{fb}$, we can obtain its gravitational mass $M_{rem,grav}$ taking into account neutrino losses. When $M_{CO} \geq 7.6 M_{\odot}$, the STARTRACK recipes request $f_{fb} = 1$ (in equation B2), i.e. the entire final mass of the star goes into

the remnant mass. This means that the direct collapse of a star into a BH occurs if $M_{CO} \geq 7.6 M_{\odot}$, according to STARTRACK prescriptions.

For NSs we use the expression given by Timmes, Woosley & Weaver (1996), for which

$$M_{rem,grav} = \frac{\sqrt{1 + 0.3 M_{rem,bar}} - 1}{0.15}. \quad (B3)$$

For BHs we use the formula

$$M_{rem,grav} = 0.9 M_{rem,bar}, \quad (B4)$$

following the approach described in Fryer et al. (2012).

B2 Rapid SN model

For the rapid SN mechanism, a fixed mass of the protocompact object, $M_{proto} = 1.0 M_{\odot}$, is assumed. In this case, the coefficient f_{fb} is given by

$$f_{fb} = \begin{cases} \frac{0.2}{M_{fin} - M_{proto}} & M_{CO} < 2.5 M_{\odot}, \\ \frac{0.286 M_{CO} - 0.514}{M_{fin} - M_{proto}} & 2.5 \leq M_{CO}/M_{\odot} < 6.0, \\ 1.0 & 6.0 \leq M_{CO}/M_{\odot} < 7.0, \\ \alpha_R M_{CO} + \beta_R & 7.0 \leq M_{CO}/M_{\odot} < 11.0, \\ 1.0 & M_{CO} \geq 11.0 M_{\odot}, \end{cases} \quad (B5)$$

where

$$\alpha_R \equiv 0.25 - \frac{1.275}{M_{fin} - M_{proto}},$$

$$\beta_R \equiv 1 - 11\alpha_R. \quad (B6)$$

This means that the direct collapse of a star into a BH occurs if $6.0 \leq M_{CO}/M_{\odot} \leq 7.0$ and if $M_{CO} \geq 11 M_{\odot}$ (equation B5), according to the rapid SN model.

B3 Delayed SN model

For the delayed SN mechanism, the prescriptions for the mass of the protocompact object are

$$M_{proto} = \begin{cases} 1.2 M_{\odot} & M_{CO} < 3.5 M_{\odot}, \\ 1.3 M_{\odot} & 3.5 \leq M_{CO}/M_{\odot} < 6.0, \\ 1.4 M_{\odot} & 6.0 \leq M_{CO}/M_{\odot} < 11.0, \\ 1.6 M_{\odot} & M_{CO} \geq 11.0 M_{\odot}. \end{cases} \quad (B7)$$

The amount of fallback is determined using the following relations:

$$f_{fb} = \begin{cases} \frac{0.2}{M_{fin} - M_{proto}} & M_{CO} < 2.5 M_{\odot}, \\ \frac{0.5 M_{CO} - 1.05 M_{\odot}}{M_{fin} - M_{proto}} & 2.5 \leq M_{CO}/M_{\odot} < 3.5, \\ \alpha_D M_{CO} + \beta_D & 3.5 \leq M_{CO}/M_{\odot} < 11.0, \\ 1.0 & M_{CO} \geq 11.0 M_{\odot}, \end{cases} \quad (B8)$$

where

$$\alpha_D \equiv 0.133 - \frac{0.093}{M_{fin} - M_{proto}},$$

$$\beta_D \equiv 1 - 11\alpha_D. \quad (B9)$$

Thus, the direct collapse of a star into a BH occurs if $M_{CO} \geq 11 M_{\odot}$ (equation B8), according to the delayed SN model (i.e. the same as the rapid SN model, but significantly larger than in the STARTRACK recipes).

APPENDIX C: GENERAL FITTING FORMULA FOR M_{rem}

We report a fitting formula that expresses the compact remnant mass M_{rem} as a function of M_{ZAMS} and Z . The following formula has been obtained by fitting the outputs of SEVN with the delayed SN model and the PARSEC stellar evolution isochrones. The value of M_{rem} obtained with the fitting formula deviate from the outputs of SEVN by $\lesssim 10$ per cent.

First, we express M_{rem} as a function of M_{CO} and Z (from Fig. 7). For $Z \leq 5.0 \times 10^{-4}$, the best-fitting curve for M_{rem} is given by

$$M_{\text{rem}} = \begin{cases} \max(p(M_{\text{CO}}), 1.27 M_{\odot}) & \text{if } M_{\text{CO}} \leq 5 M_{\odot}, \\ p(M_{\text{CO}}) & \text{if } 5 < M_{\text{CO}}/M_{\odot} < 10.0, \\ \min(p(M_{\text{CO}}), f(M_{\text{CO}}, Z)) & \text{if } M_{\text{CO}} \geq 10 M_{\odot}, \end{cases} \quad (\text{C1})$$

where

$$p(M_{\text{CO}}) = -2.333 + 0.1559 M_{\text{CO}} + 0.2700 M_{\text{CO}}^2, \quad (\text{C2})$$

$$f(M_{\text{CO}}, Z) = m(Z) M_{\text{CO}} + q(Z),$$

with coefficients

$$m(Z) = -6.476 \times 10^2 Z + 1.911, \quad (\text{C3})$$

$$q(Z) = 2.300 \times 10^3 Z + 11.67.$$

For $Z > 5.0 \times 10^{-4}$ we have

$$M_{\text{rem}} = \begin{cases} \max(h(M_{\text{CO}}, Z), 1.27 M_{\odot}) & \text{if } M_{\text{CO}} \leq 5 M_{\odot}, \\ h(M_{\text{CO}}, Z) & \text{if } 5 < M_{\text{CO}}/M_{\odot} < 10.0, \\ \max(h(M_{\text{CO}}, Z), f(M_{\text{CO}}, Z)) & \text{if } M_{\text{CO}} \geq 10 M_{\odot}, \end{cases} \quad (\text{C4})$$

where

$$h(M_{\text{CO}}, Z) = A_1(Z) + \frac{A_2(Z) - A_1(Z)}{1 + 10^{(L(Z) - M_{\text{CO}})\eta(Z)}}, \quad (\text{C5})$$

$$f(M_{\text{CO}}, Z) = m(Z) M_{\text{CO}} + q(Z).$$

For $Z \geq 1.0 \times 10^{-3}$, the coefficients of the function $h(M_{\text{CO}}, Z)$ are

$$A_1(Z) = 1.340 - \frac{29.46}{1 + \left(\frac{Z}{1.110 \times 10^{-3}}\right)^{2.361}},$$

$$A_2(Z) = 80.22 - 74.73 \frac{Z^{0.965}}{2.720 \times 10^{-3} + Z^{0.965}},$$

$$L(Z) = 5.683 + \frac{3.533}{1 + \left(\frac{Z}{7.430 \times 10^{-3}}\right)^{1.993}},$$

$$\eta(Z) = 1.066 - \frac{1.121}{1 + \left(\frac{Z}{2.558 \times 10^{-2}}\right)^{0.609}}, \quad (\text{C6})$$

while for $Z < 1.0 \times 10^{-3}$, the coefficients of the function $h(M_{\text{CO}}, Z)$ are

$$A_1(Z) = 1.105 \times 10^5 Z - 1.258 \times 10^2,$$

$$A_2(Z) = 91.56 - 1.957 \times 10^4 Z - 1.558 \times 10^7 Z^2,$$

$$L(Z) = 1.134 \times 10^4 Z - 2.143,$$

$$\eta(Z) = 3.090 \times 10^{-2} - 22.30 Z + 7.363 \times 10^4 Z^2. \quad (\text{C7})$$

For $Z \geq 2.0 \times 10^{-3}$, the coefficients of the function $f(M_{\text{CO}}, Z)$ are independent of Z :

$$m = 1.217, \quad q = 1.061, \quad (\text{C8})$$

while, for $1.0 \times 10^{-3} \leq Z < 2.0 \times 10^{-3}$ we have

$$m = -43.82 Z + 1.304, \quad q = -1.296 \times 10^4 Z + 26.98 \quad (\text{C9})$$

and for $Z < 1.0 \times 10^{-3}$ we have

$$m = -6.476 \times 10^2 Z + 1.911, \quad q = 2.300 \times 10^3 Z + 11.67. \quad (\text{C10})$$

Furthermore, M_{CO} can be expressed as a function of M_{ZAMS} and Z , by fitting the curves of Fig. 5. The functional form of the fit is

$$M_{\text{CO}} = -2.0 + [B_1(Z) + 2.0] [g(Z, M_{\text{ZAMS}}; K_1, \delta_1) + g(Z, M_{\text{ZAMS}}; K_2, \delta_2)], \quad (\text{C11})$$

where

$$g(Z, M_{\text{ZAMS}}; x, y) \equiv \frac{0.5}{1 + 10^{(x(Z) - M_{\text{ZAMS}})y(Z)}}. \quad (\text{C12})$$

For $Z > 4.0 \times 10^{-3}$ the coefficients are

$$B_1(Z) = 59.63 - 2.969 \times 10^3 Z + 4.988 \times 10^4 Z^2,$$

$$K_1(Z) = 45.04 - 2.176 \times 10^3 Z + 3.806 \times 10^4 Z^2,$$

$$K_2(Z) = 1.389 \times 10^2 - 4.664 \times 10^3 Z + 5.106 \times 10^4 Z^2,$$

$$\delta_1(Z) = 2.790 \times 10^{-2} - 1.780 \times 10^{-2} Z + 77.05 Z^2,$$

$$\delta_2(Z) = 6.730 \times 10^{-3} + 2.690 Z - 52.39 Z^2. \quad (\text{C13})$$

For $1.0 \times 10^{-3} \leq Z \leq 4.0 \times 10^{-3}$, we have

$$B_1(Z) = 40.98 + 3.415 \times 10^4 Z - 8.064 \times 10^6 Z^2,$$

$$K_1(Z) = 35.17 + 1.548 \times 10^4 Z - 3.759 \times 10^6 Z^2,$$

$$K_2(Z) = 20.36 + 1.162 \times 10^5 Z - 2.276 \times 10^7 Z^2,$$

$$\delta_1(Z) = 2.500 \times 10^{-2} - 4.346 Z + 1.340 \times 10^3 Z^2,$$

$$\delta_2(Z) = 1.750 \times 10^{-2} + 11.39 Z - 2.902 \times 10^3 Z^2. \quad (\text{C14})$$

Finally, for $Z < 1.0 \times 10^{-3}$, the coefficients do not depend on Z :

$$B_1 = 67.07, \quad K_1 = 46.89, \quad K_2 = 1.138 \times 10^2,$$

$$\delta_1 = 2.199 \times 10^{-2}, \quad \delta_2 = 2.602 \times 10^{-2}. \quad (\text{C15})$$

This paper has been typeset from a \LaTeX file prepared by the author.